Coherent Tracer Correlations in Deep-sea Corals and Implications for Biomineralization Mechanisms underlying Vital Effects

Sang Chen (sang@sjtu.edu.cn)[1,2], *Eloise F.M. Littley*[3], *James W.B. Rae*[3], *Christopher D. Charles*[4], *Yunbin Guan*[2], *Jess F. Adkins*[2]

1. School of Oceanography, Shanghai Jiao Tong University, Shanghai, China 200030
2. Division of Geological and Planetary Sciences, California Institute of Technology, Pasadena, CA 91125, USA
3. School of Earth and Environmental Sciences, University of St Andrews, St Andrews, UK
4. Scripps Institution of Oceanography, University of California San Diego, La Jolla, CA 92093, USA

Abstract

Deep-sea corals are a useful archive of thermocline, intermediate, and deep waters in past oceans. However, application of traditional oceanographic tracers to deep-sea corals remains a challenge due to our insufficient understanding of their “vital effects”. Deep-sea corals are ideal test organisms to study the mechanism underlying vital effects generally, due to the large tracer gradients in individual corals living under relatively constant environmental conditions. Lessons learned from these corals might apply to other scleractinia and to marine calcifiers more generally. Here we present stable isotope, minor and trace metal (Me/Ca ratios) data in a suite of modern *Desmophyllum dianthus* specimens, collected over multiple spatial scales in individual corals (bulk, micromill, SIMS, NanoSIMS), with multi-proxy analyses made on the same material whenever possible. Spatially coherent Me/Ca correlations are observed in the fibrous aragonite of individual corals, including positive correlations between Mg/Ca, Li/Ca and B/Ca, as well as negative correlations between Mg/Ca and Sr/Ca, consistent with previous studies. We also for the first time document strong correlations between the isotopic (δ^{18}O and δ^{13}C) and elemental compositions of the skeletons, most notably a negative correlation between δ^{18}O and Mg/Ca. The centers of calcification (COCs) in the coral skeletons show distinct tracer correlations from the aragonite fibers that possibly reflect a more complicated formation mechanism. We interpret the spatially coherent tracer correlations in deep-sea corals with a numerical model of coral calcification previously developed for stable isotopes that considers the role of the enzyme carbonic anhydrase in the calcification processs. With the carbonate chemistry in the model constrained by the stable isotope data, we are able to explain the observed Me/Ca correlations as well as their range of variability, as a result of internal pH elevation in the extracellular calcifying fluid (ECF) of the corals with limited Ca-pumping through the calicoblastic membrane. In particular, the positive Mg/Ca–B/Ca correlation in the fibrous aragonite suggests a borate ($B(OH)_4^-$) substitution for carbonate ion (CO_3^{2-}) incorporation mechanism in biogenic aragonite. We also suggest the growth rate dependence of the incorporation of minor and trace elements based conceptually on an ion-by-ion growth model may help explain the absolute Me/Ca values in biogenic aragonites. Finally, we generally find more limited tracer variability in corals from undersaturated seawater compared to their counterparts from supersaturated conditions, suggesting a limit to their internal pH elevation in response to this environmental stress. Understanding the biomineralization mechanisms underlying the vital effects is important for better use of these tracers for paleoceanographic applications, and may shed light on the response of marine calcification to future ocean acidification.

Key words: Deep-sea Corals; Oxygen and Carbon Isotopes; Minor/Trace Elements; Vital Effects; Internal pH Elevation; Growth Rate Dependence

1. Introduction

Deep-sea scleractinian corals are an emerging archive of intermediate and deep water conditions in the ocean. Over the past few decades, numerous isotopic and elemental tracers have been developed in deep-sea corals to reconstruct the temperature, carbonate chemistry, nutrient status, and circulation changes in the deep ocean during key climate events of the last glacial period as well as the Holocene , and reveal the close coupling between ocean dynamics, biogeochemistry and the global carbon cycle (Smith et al., 1997; Adkins et al., 1998; Goldstein et al., 2001; Frank et al., 2004; Robinson et al., 2005; Montero-Serrano et al., 2013; Thiagarajan et al., 2014; Wang et al., 2017; Bonneau et al., 2018; Rae et al., 2018; Elliot et al., 2019; Hines et al., 2019; Li et al., 2020; Wilson et al., 2020). Despite the substantial progress made in using this archive, applications of traditional paleoceanographic tracers such as oxygen and carbon isotopes and Mg/Ca and Sr/Ca thermometers remain a challenge due to our incomplete understanding of these tracers in terms of both empirical calibrations and the underlying biomineralization mechanisms.

In addition to their use as a paleoceanographic archive, deep-sea corals are ideal test organisms to study the biomineralization process due to their relatively constant growth environment and the large range of tracer variability within individual corals (Adkins et al., 2003; Rollion-Bard et al., 2003; Robinson et al., 2006; Gagnon et al., 2007; Case et al., 2010; Rollion-Bard et al., 2010; Robinson et al., 2014; Rollion-Bard and Blamart, 2015; Stewart et al., 2016). The variability in tracers has been associated with different growth structures (COCs vs. aragonite fibers), and attributed to the internal pH elevation process in the ECF of the corals (Adkins et al., 2003; Rollion-Bard et al., 2003; Chen et al., 2018). The internal pH elevation through membrane-bound Ca^{2+} and proton transporters has been observed in a variety of marine calcifying organisms (Al Horani et al., 2003; Zoccola et al., 2004; de Nooijer et al., 2009; Venn et al., 2011; Toyofuku et al., 2017), and is likely a common mechanism for vital effects in geochemical tracers in biogenic carbonates. In corals, the depletions in $\delta^{18}O$ and $\delta^{13}C$ from equilibria have been explained by the kinetic isotope effects of $CO_2(aq)$ hydration and carbon source mixing (McConnaughey, 1989a, b;

Adkins et al., 2003; Rollion-Bard et al., 2003, 2010, 2011; Chen et al., 2018), while the variability in Me/Ca ratios has been interpreted with the Rayleigh distillation process associated with Ca^{2+} dynamics (Gagnon et al., 2007; Gaetani et al., 2011) or possible kinetic effects associated with growth rates (Sinclair, 2005; Sinclair and Risk, 2006; Rollion-Bard and Blamart, 2015). However, few studies to date have tried to directly link stable isotopes and Me/Ca ratios to get a coherent and quantitative understanding of biomineralization and its imprint on vital effects in different tracers (Allison et al., 2010; Stewart et al., 2016; Wu et al., 2017; Chen et al., 2021).

Here we present an effort to mechanistically link the stable isotopes and Me/Ca ratios in the deep-sea coral species *D. dianthus*, through observations across different spatial scales and a numerical model of coral calcification. Observations of stable isotopes and Me/Ca ratios are made on NanoSIMS (a few μm), SIMS (tens of μm), micromill (100 μm) and bulk (mm–cm) scales in individual corals and consistent tracer correlations are found through these scales. The numerical model was previously developed to explain the stable isotope vital effects in deep-sea corals as well as other marine calcifying organisms (Chen et al., 2018). The model is able to explain the range in $\delta^{18}O$ and $\delta^{13}C$ variability in individual corals and the strong $\delta^{18}O$–$\delta^{13}C$ correlation via carbonate chemistry changes in the ECF through internal pH elevation. In particular, we found that the slope of the $\delta^{18}O$–$\delta^{13}C$ correlation is modulated by the activity of carbonic anhydrase in the calcification process. Carbonic anhydrase activity couples $\delta^{18}O$ and $\delta^{13}C$ by controlling two important and internally linked processes: the hydration kinetics of $CO_2(aq)$ in the ECF and therefore the cross-membrane $CO_2(aq)$ flux into the ECF from the calicoblastic cells. The hydration kinetics of $CO_2(aq)$ relative to $CaCO_3$ precipitation determines the magnitude of ^{18}O kinetic isotope effects preserved in the skeleton, while the cross-membrane $CO_2(aq)$ flux determines the mixing ratio of ^{13}C-enriched seawater DIC and ^{13}C-depleted cell $CO_2(aq)$. In this way the presence of carbonic anhydrase makes the slope of skeletal $\delta^{18}O$ vs. $\delta^{13}C$ an emergent property of the biomineralization process (Chen et al., 2018). By fitting the stable isotope data, the model also constrains the carbonate chemistry of the calcifying fluid that can influence tracers sensitive to these changes. Another important aspect of the stable isotope model is the incorporation of the growth rate dependence of isotope fractionation based on an ion-by-ion growth model (Watkins et al., 2013, 2014), through which we find an agreement between the equilibrium isotopic end member in deep-sea corals and inorganic precipitation experiments. In this study, we attempt to extend these aspects of the stable isotope model to the minor and trace elements to explore the key biomineralization processes underlying vital effects in deep-sea corals, and the degree to which these vital effects can be explained with fundamental physicochemical principles. By understanding the relevant biomineralization processes, we also make a preliminary attempt to explore the response of the biomineralization process to changes in the ambient environment and its implications for empirical tracer calibrations.

2. Methods

2.1 Sample Preparation

The *D. dianthus* specimens used in this study were either provided by the Smithsonian Museum of Natural History or collected from Seamounts south of Tasmania with the deep submergence vehicle Jason during cruise TN-228 in 2008–2009 on the R/V Thompson. A list of the coral specimens and their estimated growth environmental conditions can be found in Chen et al. (2021) as well as the Supplementary Material. Most corals were collected with tissue remains attached and therefore considered modern. For bulk measurements, a small piece containing both the septa and theca was removed from each coral calice, rinsed with ethanol and DI water, dried with compressed air and crushed with a mortar and pestle before chemical processing. To sample different growth features in the coral skeleton, a piece of the skeleton was cut from the top view of a coral calice that comprises a few septa joined by the theca wall (Figure 1). The cut piece was mounted on a 1'' glass slide, and a Buehler Isomet low speed water saw with a 0.3 mm diamond wafer blade was used to slice off the top to make a thick section. The removed top of the cut piece was then mounted on a different glass slide to make extra thick sections. The sections were hand polished on 3M lapping films with sequentially finer grating down to 1 µm grain size. For micromilling purposes, the sections were kept at ~1 mm thick. For SIMS and NanoSIMS analyses, the sections were polished down to ~100 µm thickness and further smoothed vibrationally on a polishing cloth with 30 nm colloidal silica. Reflected and transmitted light images were acquired for the sections with a Leica DM 2500P modular polarizing microscope, as well as a Q-imaging micropublisher 5.0 ETV camera mounted on an Olympus SZ-CTV microscope (Figure 1).

2.2 Micromilled Samples

The micromilling procedure is similar to that used in Adkins et al. (2003) and Gagnon et al. (2007), and detailed in Chen et al. (2021). In brief, we used a computer controlled Merchantek Micromill system, with the goal of making powders of coral growth bands that can be measured for stable isotopes ($\delta^{13}C$ and $\delta^{18}O$) as well as Me/Ca ratios. For stable isotopes, the collected sample powders (30–100 µg) were transferred to Kiel device vials and analyzed on a Finnigan MAT 253 mass spectrometer coupled to a Kiel IV device at Scripps Institution of Oceanography.

The Me/Ca ratios of the samples (50–200 µg) were measured in two different labs at the University of St Andrews and the California Institute of Technology. The general procedure of sample processing is similar between the two labs and has been previously described in Chen et al. (2021). A cleaning test was performed at University of St Andrews by measuring splits of the same powder, one of which was uncleaned, while the other was sequentially cleaned by 0.1M NH_4OH+1% H_2O_2 and 0.0005M HNO_3 solutions. It was found that chemical cleaning would cause approximately 1/3 loss of sample powder and tend to reduce Me/Ca variability in individual corals observed with other techniques, suggesting presence of a more soluble phase in the sample powder. A similar observation can be made on the Jcp-1 standard, as chemical cleaning of the powder lowers Me/Ca systematically compared to uncleaned powder (Table 1). To better preserve the Me/Ca variability and compare to other observation techniques, most of the samples were directly dissolved in 150–300 μL 5% HNO_3 (depending on sample size) without chemical cleaning before ICP-MS analyses.

The Me/Ca analyses were performed on an Agilent 7500a ICP-MS at St Andrews, and an Agilent 7500cx ICP-MS at Caltech. Both instruments used an inert sample introduction system with a Teflon spray chamber and sapphire injector, and used a 3% HNO_3+1% HF solution as a rinse between samples in order to reduce the build-up of boron blanks during an analytical session (Zeebe and Rae, 2020). A slightly different set of isotopes were collected between the two labs, but both methods include ^{7}Li, ^{11}B, ^{24}Mg, ^{25}Mg, ^{27}Al, ^{43}Ca, ^{48}Ca, ^{55}Mn, ^{88}Sr, ^{111}Cd, ^{138}Ba and ^{238}U. The samples were measured with 3 internal cycles at St Andrews and 4 at Caltech. The Me/Ca intensity ratios were converted to molar ratios by bracketing with in-house calibration standards that are gravimetric mixtures of single element solutions. A recently developed standard solution, NIST8301(Coral) (abbreviated as 8301C below), was used as the calibration standard at Caltech, and was used to correct for Me/Ca ratios of the bracketing standard at St Andrews, in both cases based on interlab values published in Stewart et al. (2021). The coral standard Jcp-1 (Hathorne et al., 2013) was measured together with other in-house consistency standards in each analytical session to check for accuracy and instrumental drift. Since not all elements measured with wet chemistry can be measured accurately and precisely with SIMS and NanoSIMS, this paper focuses on the common elements Li, B, Mg, Ca and Sr. Note that Me/Ca of bulk *D. dianthus* powder samples (i.e. large samples, distinct from micromilled bands) were also measured with the same method at Caltech (sample preparation detailed in Chen et al., 2021), and are referenced in the following discussions, with more details to be presented in future work.

Table 1 lists the calibrated Li/Ca, B/Ca, Mg/Ca and Sr/Ca ratios of Jcp-1. Our ratios at both Caltech and St Andrews for the uncleaned Jcp-1 powder are generally within the uncertainties of the interlab calibrated values reported by Hathorne et al. (2013), suggesting good accuracy agreement between the Jcp-1 and 8301C standards. The Sr/Ca ratios of Jcp-1 measured at Caltech and St Andrews are 1.7% and 1.1% lower than the interlab value in Hathorne et al. (2013) respectively. The magnitude of this offset is within 1σ of the interlab variations (1.7%) for 8301C in Stewart et al. (2021), but is reproducible and warrants further laboratory testing. A previous study using a similar method measured a larger Sr/Ca offset (4.7%) in Jcp-1 from the interlab value (Stewart et al., 2016), suggesting such offsets are not uncommon for Sr/Ca. We apply these offsets to our Sr/Ca data, but do not correct for the other Me/Ca ratios. Based on standard deviations of replicate measurements of the standard solutions or average standard deviations of our samples (whichever is greater), the analytical uncertainties for our Li/Ca, B/Ca, Mg/Ca and Sr/Ca ratios are 1.4%, 1.9%, 0.6% and 0.6% respectively.

2.3 SIMS measurements

The SIMS measurements were performed on a Cameca ims 7f-Geo instrument at the Caltech Microanalysis Center with a method modified from Gabitov et al. (2013). The prepared

D. dianthus sections were rinsed with DI water and isopropanol and coated with 20 nm gold before being loaded into the instrument. A –12.5 keV primary O^- beam of 5–6.5 nA and ~25–30 μm in size was used to sputter the sample surface to generate secondary ions to achieve sufficient spatial resolution and signal intensity for the trace elements. Positive (+9 keV) secondary ions of ^{7}Li, ^{11}B, ^{26}Mg, ^{42}Ca and ^{88}Sr were collected, with a field aperture of 300 μm, a contrast aperture of 250 μm, an energy bandwidth of 45 eV, and an entrance/exit slits setting corresponding to a mass resolving power (MRP) of 3000. This MRP is sufficient to resolve molecular interferences (mostly hydrides) on the elements of interest, except for $^{87}SrH^+$ and $^{44}Ca_2^+$ on $^{88}Sr^+$, which would require an MRP over 8000 and thus significantly reduce the transmission signals for other secondary ions. However, our high-MRP mass scan indicated that $^{87}SrH^+$ and $^{44}Ca_2^+$ contribute less than 1% to the $^{88}Sr^+$ peak intensity.

Each spot on the sample was pre-sputtered for 1 minute before data collection with the same primary beam intensity. The secondary ions were measured for 30–40 cycles on each spot, and each cycle consisted of 3 seconds of counting for ^{7}Li, 5s for ^{11}B, and 1s each for ^{26}Mg, ^{42}Ca and ^{88}Sr. A waiting time of 2–7s was applied between the mass peak jumps of the magnet. All secondary ions were detected with an ETP electron multiplier (EM) and corrected for the EM deadtime. The typical count rate was 100–200 cps for ^{7}Li and ^{11}B, 6,000–7,000 cps for ^{26}Mg, 80,000–100,000 cps for ^{42}Ca and 100,000–120,000 cps for ^{88}Sr. The relative standard errors for each spot generally follow counting statistics, with ~1% for Li/Ca and B/Ca, ~0.5% for Mg/Ca and ~0.2% for Sr/Ca. Although Sr/Ca ratios of individual spots show larger variability compared to counting statistics expectations (0.1%), likely due to interferences and sample charging, the errors are still small enough to resolve natural Sr/Ca variability in the coral skeletons.

The carbonatite standard OKA was used to calibrate Mg/Ca and Sr/Ca ratios in the samples. This standard has Mg/Ca (4.67±0.15 mmol/mol) and Sr/Ca (19.43±0.76 mmol/mol) ratios close to those of corals, and Gabitov et al. (2013) identified a relatively homogeneous matrix region that was ideal for accuracy calibration. 2–3 spots on the standard were measured between samples during each analytical session, and only Mg/Ca and Sr/Ca measurements from the homogeneous matrix region were used for calibration. For Li/Ca and B/Ca, no well documented carbonate standard was available at Caltech during the analytical sessions. A calibration attempt was made by measuring a series of USGS glass standards with a wide range in Li/Ca and B/Ca (Jochum et al., 2006). Although the glass-based Li/Ca and B/Ca calibrations are self-consistent, applying them to the corals caused a strong deviation of the elemental ratios (approximately a factor of 2 for Li, a factor of 3 for B) from those measured by wet chemistry, suggesting strong matrix-dependence of the ionization efficiency of these elements between carbonates and silicate glass. To make the SIMS measurements comparable to the wet chemistry measurements, we chose one *D. dianthus* specimen as the calibration reference for all the other samples to build an internally consistent Li/Ca and B/Ca calibration. Coral 80358 from North Atlantic was chosen because its average Mg/Ca and Sr/Ca from all measured SIMS spots (independently calibrated by OKA) most closely match those of the bulk powder measured by wet chemistry (2.3% difference in Mg/Ca, 4.5% difference in Sr/Ca). As a result, the average Li/Ca and B/Ca of all measured SIMS spots on 80358 are assigned the Li/Ca and B/Ca elemental ratios of the bulk powder, assuming the SIMS spots have sampled skeletal structures representative of the bulk powder. Although this assumption may cause inaccuracies in absolute Li/Ca and B/Ca ratios at the few percent level, we do not expect a major influence on our interpretations of the biomineralization mechanisms, because the range of Li/Ca and B/Ca variability in individual corals is much larger than this possible offset, and the same accuracy offset applies to all spots from an individual coral so that the relative Me/Ca changes stay the same within each individual.

In addition to Me/Ca measurements with the O^- source, we also carried out $\delta^{18}O$ measurements on the corals with the Cs^+ source of the same SIMS instrument. The measurements were made with a +10 keV Cs^+ beam and a primary ion current of ~3 nA. The method used a field aperture of 300 μm, a contrast aperture of 400 μm, an energy bandwidth of 45 eV, and an entrance/exit slits setting corresponding to an MRP of 1500. Negative (–9 KeV) secondary ions of ^{16}O and ^{18}O were collected with two separate Faraday Cups (FC1 and FC2). Sample charging was compensated with a –9 keV electron gun. On each spot, sample was first pre-sputtered for 120 seconds to remove gold coating and possible surface contamination. Then secondary ions of ^{16}O and ^{18}O were measured for 1s each in the peak-jumping mode (with 1s waiting time in between) for 50 cycles. The internal standard errors of the $\delta^{18}O$ measurements are approximately 0.5‰. The measured $^{18}O/^{16}O$ ratios are converted to the VPDB scale with two in-house $CaCO_3$ standards of known $\delta^{18}O$ compositions (UWC3 with $\delta^{18}O$ of –17.87‰, 46E1436 with $\delta^{18}O$ of –8.99‰). Measurements of multiple spots on each standard yield external standard errors of 0.5‰, consistent with the internal standard errors of individual spots. In order to correlate $\delta^{18}O$ and Me/Ca ratios, parallel lines of spots were measured for Me/Ca and $\delta^{18}O$ respectively. While the precision of the $\delta^{18}O$ measurements is far from optimum, we find similar Me/Ca–$\delta^{18}O$ relations in the SIMS measurements when compared to other observation scales, as discussed in the following sections.

2.4 NanoSIMS element mapping

We used the imaging mode of a Cameca NanoSIMS 50-L instrument at the Caltech Microanalysis Center to map the distribution of Li, B, Mg, Ca and Sr in individual *D. dianthus*. Ion images of positive (+8 keV) secondary ions were generated with a negative (–8 KeV) $^{16}O^{-}$ primary beam of a few to tens of pA rastering over areas of 30×30 μm or 40×40 μm. With a spatial resolution of ~200-400 nm under such setup, the NanoSIMS mapping is expected to resolve Me/Ca variability on the scale of a few hundred aragonite unit cells. To remove surface contamination, 30–60 minutes of pre-sputtering with a larger beam (~1 nA) was applied before image collection. Then ion images of 512×512 pixels were collected with dwell time of 5–15 ms/pixel. One imaging frame takes ~20-60 minutes. To strengthen the signals of the trace elements, multiple image frames were collected on each spot to accumulate as many counts as possible for the trace elements and reduce the noise in the images.

The raw data were loaded into Matlab with the package Look@NanoSIMS (Polerecky et al., 2012) for further image processing, such as averaging, smoothing and Me/Ca ratio calculations. The L'IMAGE (Larry Nittler) software was used to generate Me/Ca transects across the images. Due to a lack of charging compensation when sputtering nonconductive samples (like corals) with an O^{-} beam, especially on a large area (40×40 um) and with a large beam current (tens of pA), sample charging became significant during NanoSIMS imaging. During our analytical sessions, we found it generally difficult to generate images with relatively uniform Ca intensity on our coral samples, especially on the edges of a spot, therefore complicating all Me/Ca patterns. Using a smaller beam current increases Ca uniformity, but also cuts the signal intensity for all the secondary ions, which becomes an issue for trace elements. Therefore the discussion below will focus on the spots that were collected for sufficient time (minimum 4 frames) and show a reasonable degree of uniformity in Ca intensity (<30% variability). The same method and data processing was used on the OKA standard to calibrate our Mg/Ca and Sr/Ca ratios. To calibrate our Li/Ca and B/Ca ratios, we assumed the average values of our Me/Ca profiles equal those of the bulk composition of each coral.

3. Results

3.1 Stable Isotopes

The $\delta^{18}O$ and $\delta^{13}C$ of the micromilled *D. dianthus* samples are shown in Figure 2. As with previous studies (McConnaughey, 1989a; Smith et al., 2002; Adkins et al., 2003; Blamart et al., 2005), we see a wide range of $\delta^{18}O$ and $\delta^{13}C$ values in individual corals and a linear $\delta^{18}O$–$\delta^{13}C$ correlation with slopes in the range of 1.9–2.7. The COCs or COC-like structures show slight deviations from the trend defined by the fibrous aragonite with generally more deplected $\delta^{18}O$ and $\delta^{13}C$ values, consistent with previous observations (Adkins et al., 2003; Blamart et al., 2005; Rollion-Bard et al., 2010). However, the deviations are not as clear for most corals in this study as those in Adkins et al. (2003), and the sampled COC bands do not always have the most depleted values in individual corals (e.g. BigBeauty, 48744, Titan-b and Titan-t). We attribute this to the micromilling procedure used in this study, which targeted larger amounts of aragonite material for coupled stable isotope and Me/Ca measurements. Given the textural heterogeneities in *D. dianthus* skeletons over micrometer scales, micromilling larger amounts of powder could cause more averaging of the isotopic and elemental compositions of the samples, and mitigate the distinction between COCs and fibrous aragonite. However, we still see consistent linear $\delta^{18}O$–$\delta^{13}C$ correlation patterns in each individual coral with a narrow range of slopes, suggesting a common biomineralization process of internal pH elevation modulated by carbonic anhydrase as modeled in Chen et al. (2018). In light of the Chen et al. (2018) model, we also observe a difference in the range of δ^{18}O and δ^{13}C values in individual corals with respect to aragonite saturation states in the ambient seawater (Figure 2)., We find that corals from undersaturated environments ($\Omega_A = [Ca^{2+}]_{sw}[CO_3^{2-}]_{sw}/K_{sp}^{arag} < 1$) generally have a narrower range of δ^{18}O and δ^{13}C values, while corals from supersaturated environments ($\Omega_A > 1$) are capable of reaching more extreme isotopic depletions. Since the δ^{18}O and δ^{13}C range is determined by the magnitude of pH elevation, this difference in range suggests different amount of pH elevation in individual corals in response to the saturation state of the seawater, which will be further discussed below.

3.2 Me/Ca correlations from micromill and SIMS

Strong correlations in the fibrous aragonite of *D. dianthus* have been previously observed for Li/Ca, Mg/Ca and Sr/Ca, with COCs showing distinct relations for these elements (Gagnon et al., 2007; Case et al., 2010; Rollion-Bard and Blamart, 2015). Possible correlations were also suggested for these elements with B/Ca and boron isotopes in *D. dianthus*, although the previous data were too scarce to evaluate the significance of such correlations (Stewart et al., 2016; Wu et al., 2017). Examples of Me/Ca correlations from our micromilled samples and SIMS measurements are shown in Figure 3 and 4 respectively. Unfortunately a significant fraction of the Li/Ca ratios of the micromilled samples are unrealistically high for corals, most likely due to contamination introduced during the micromilling process. The contamination is not significant for B, Mg and Sr given good agreement between micromill, SIMS and bulk measurements.

From the micromilled samples, we see that Mg/Ca and B/Ca are generally positively correlated while Mg/Ca and Sr/Ca are negatively correlated in the aragonite fibers of the corals (Figure 3). The COC regions generally have the highest Mg/Ca in each coral, with intermediate to low Sr/Ca and B/Ca ratios, and do not have the same Me/Ca correlations as the fibers. However, there is significant scatter for these Me/Ca correlations in the micromill data, which is largely cleaned up in more spatially resolved SIMS measurements (Figure 4).

For the SIMS data on the four corals shown in Figure 4, we see cleaner positive Mg/Ca–Li/Ca and negative Mg/Ca–Sr/Ca correlations in the aragonite fibers, with COCs often deviating from the trends, consistent with previous studies (Gagnon et al., 2007; Case et al., 2010; Rollion-Bard and Blamart, 2015). While COCs generally have higher Mg/Ca and Li/Ca than the fibrous aragonite, their Sr/Ca values are highly variable between (and even within) individual corals. Among the COCs sampled in these corals, the Sr/Ca of COCs can be of low (80358-S1, 47407-S1, BigBeauty-S1), intermediate (80358-S2, 47407-S2) or high (Gaia) values compared to the fibers. This phenomenon is difficult to fathom with a simple biomineralization mechanism, but seems to be very reproducible (Gagnon et al., 2007; Stewart et al., 2016) and is worth further investigation. The positive Mg/Ca–B/Ca correlation in the aragonite fibers is much more obvious in the SIMS data than in the micromilled data, with COCs showing an opposite correlation of higher Mg/Ca and lower B/Ca, forming an overall arch-shaped correlation. We consistently observe this relation in different corals with SIMS measurements, suggesting a strong coupling of B and Mg incorporation in the fibrous aragonite and possibly a different mechanism for these elements in the COCs. We also note that the different Me/Ca correlation patterns between COCs and fibers are usually most pronounced when sampling pure septa material that is farther away from the theca, in which case the COCs and fiber bands can be easily distinguished (Figure 4). Tracer correlations in the theca regions are highly dependent on the location and properties of materials sampled, with optically dense COC-like materials (usually in the middle of theca) showing septa COC compositions and trends (80358 and Gaia), while dark fibrous theca materials (usually on the edge of theca) showing compositions and trends similar to the septa fibers (47407 and BigBeauty). This spatial heterogeneity is relevant for our micromilled samples, since the amount of materials needed to make coupled isotope and Me/Ca measurements entailed us to sample closer to the wider base of the septa that is close to the theca. Given the relatively clean Me/Ca correlation patterns in the SIMS data (Figure 4), the scatter in the micromill data (Figure 3) may be a result of mixing of COC-like structures and fibrous aragonite on small spatial scales during the sampling process, with the different Me/Ca correlations in COCs and fibers complicating the trends. Finally, it is noted in Figure 3 that Gaia, a coral from 2395 m depth in Tasmania with strong ambient undersaturation, has similar Me/Ca correlations but lower absolute Me/Ca values compared to other corals from supersaturated seawater (Figures 3, 4), suggesting possible influence of the saturation state of the seawater on the biomineralization process and thus tracer variability.

3.3 NanoSIMS element mapping

With NanoSIMS mapping, we are examining the element distribution in *D. dianthus* within the scale of a single SIMS spot as shown in Figure 1d. Figure 5 shows Me/Ca images of four 30×30 or 40×40 μm element maps from the septa of coral 62309 and 47407, one exclusively from the fibrous aragonite and the other covering COC features for each coral. Figure 6 shows 30-pixel-wide Me/Ca transects from the NanoSIMS images. The COCs show up clearly with high Mg/Ca relative to the fibers (Figure 5g, o, Figure 6f, h). As with Mg/Ca, Li/Ca is also elevated in the COCs, although the COC features are not as obvious due to the low signal intensities for Li (Figure 5e, m, Figure 6b, d). In contrast, B/Ca shows a sharp decrease into the COCs, which is especially clear in the 47407 spot (Figure 5n, 6d). Sr/Ca decreases toward the COC in the 62309 spot (Figure 5h, 6f), while it is influenced by charging effects on the edge with unreasonably high values in 47407 (Figure 5l, 5p, 6h). Outside the COCs in the fibrous aragonite, we see quasi-rhythmic Me/Ca bands that are a few μm thick with significant Me/Ca variations (50% in Li/Ca, B/Ca and Mg/Ca, 20% in Sr/Ca), which is best exemplified by the Mg/Ca bands in both corals (Figure 5c, g, k, o). As with correlations observed in the SIMS and micromill data, we see that high Mg/Ca bands are generally collocated with bands of high Li/Ca, high B/Ca and low Sr/Ca in the fibrous aragonite. The coherent Me/Ca correlations on different measurement scales suggest fine control on the incorporation of these elements during the biomineralization process.

3.4 *Me/Ca-isotope correlations*

By coupling Me/Ca measurements with stable isotopes, we aim to understand the incorporation of minor and trace elements in coral skeletons based on our mechanistic interpretation of the stable isotope patterns as a function of internal pH elevation (Adkins et al., 2003; Chen et al., 2018). Given that δ^{13}C may be slightly influenced by metabolic effects, and the strong coupling between δ^{13}C and δ^{18}O in the fibrous aragonite, we mainly use δ^{18}O as a reference metric for the internal pH elevation in the ECF. Figure 7 shows cross plots of δ^{18}O vs. Me/Ca ratios in the micromilled samples. The strongest correlation pattern is observed for Mg/Ca and δ^{18}O. In each individual coral, we see a negative Mg/Ca–δ^{18}O correlation that has a similar slope across corals (Figure 7b). Similarly, there is a negative correlation between δ^{18}O and B/Ca in the fibrous aragonite of different corals, while the COCs tend to deviate from the correlation with more depleted δ^{18}O and B/Ca values (Figure 7a). This is expected given the arch-shape Mg/Ca–B/Ca relation best exemplified in the SIMS data (Figure 4). The relationship between δ^{18}O and Sr/Ca is more complicated. A positive δ^{18}O–Sr/Ca correlation is observed in the fibrous aragonite of Gaia and 47407, while there is more scatter for 47394 and BigBeauty (Figure 7c). This is likely a result of the mixing effects during the micromilling process, which is more significant for Sr/Ca due to the aforementioned highly variable COC compositions. Notwithstanding these mixing influences on Sr/Ca, the relatively strong correlations between $\delta^{18}O$ and Me/Ca ratios in the fibrous aragonite of individual corals further suggest strong common control on these tracers by the internal pH elevation process.

4. Discussion

4.1 Tracer Correlations and Variability across Scales

With Me/Ca measurements across different spatial scales, we generally observe consistent Me/Ca correlation patterns in different *D. dianthus* individuals as summarized in Figure 8. Although direct comparison across measurement scales can be complicated by different methods and assumptions used in the Me/Ca calibrations, we see similar ranges of Me/Ca values on different measurement scales for individual corals. As it measures the smallest spatial scales, we see that the NanoSIMS data show the widest range of Me/Ca variability that is partially smoothed away in the SIMS data, and further averaged out in the micromill data (Figure 8). A similar phenomenon was observed in surface corals, with high-resolution sampling showing noisier data and weaker tracer correlations, while a certain degree of spatial averaging can enhance the correlation patterns (Sinclair, 2005). Nevertheless, we observe on different measurement scales the positive Mg/Ca–B/Ca correlation and negative Mg/Ca–Sr/Ca correlations in the fibrous aragonite of each coral, while the high Mg COCs show a different correlation, with a decrease in B/Ca and variable Sr/Ca values. Despite significant averaging, the micromill data still captures the Me/Ca variability and correlation patterns in the SIMS and NanoSIMS data. The consistent correlations and relatively high variability across scales suggest that the Me/Ca tracers are incorporated in a tightly controlled and highly dynamic biomineralization process.

The consistent tracer correlation across measurement scales not only applies to Me/Ca ratios, but also to Me/Ca and isotope correlations. Figure 9 shows the Mg/Ca–δ^{18}O correlations across measurement scales in our *D. dianthus* collection. We see linear negative Mg/Ca–δ^{18}O correlations with similar slopes in SIMS and micromill data of each individual coral. For Big Beauty, the micromill and SIMS data with independent calibration methods show the same Mg/Ca–δ^{18}O relation, although the SIMS data include points of more extreme compositions (high Mg/Ca and low δ^{18}O, Figure 9a). In addition to variations within individual corals, we also observe a similar Mg/Ca–δ^{18}O relation in our bulk coral samples (Figure 9c). This correlation strongly suggests coupling between the incorporation of isotopes and metal cations in the biomineralization process of *D. dianthus*. Finally, we note that despite similar Mg/Ca–δ^{18}O relations in different corals, the range of Mg/Ca and δ^{18}O variability is different between individuals (Figure 9b, c). Corals from supersaturated seawater generally have a wider range in Mg/Ca (2 mmol/mol) and δ^{18}O (4‰) that reach more extreme values of high Mg/Ca and low δ^{18}O, while corals from undersaturated seawater have a narrower range (1.5 mmol/mol in Mg/Ca, 3‰ in δ^{18}O). The differences point toward a response of the biomineralization process to the saturation conditions in the ambient environment.

4.2 Understanding Tracer Incorporation Mechanisms with a Numerical Biomineralization Model

4.2.1 Basic Model Setup and Behavior

The coral biomineralization model was previously developed to explain the stable isotope vital effects in deep-sea corals as well as other marine calcifying organisms (Chen et al., 2018). In addition to the stable isotope fractionation processes, the Chen et al. (2018) model also simulates the carbonate chemistry of the ECF in response to alkalinity pumping, which sets the chemical microenvironment for the incorporation of the minor and trace elements. We added equations for minor and trace elements to the previous model (Figure 10). In the model, elements such as Li, B, Mg and Sr are transported into the ECF by seawater and removed by coprecipitation with aragonite. The incorporation of these elements are coupled to Ca to calculate the Me/Ca ratios of the skeletons. The governing equations added to the model for the cations are:

$$\frac{d[Ca^{2+}]}{dt} = \frac{1}{\tau_{sw}}([Ca^{2+}]_{sw} - [Ca^{2+}]) + \frac{1}{z}(\frac{1}{2}f_{Ca}F_{Alk} - F_{CaCO_3}) \quad (1)$$

$$\frac{d[Me]}{dt} = \frac{1}{\tau_{sw}}([Me]_{sw} - [Me]) - \frac{1}{z}F_{CaCO_3}D_{Me}\frac{[Me]}{[Ca^{2+}]} \quad (2)$$

For the concentration terms, subscript "*sw*" stands for seawater, while terms without subscript represent the ECF. For the Ca and minor/trace element "Me", there is a seawater flushing term with a timescale of τ_{sw}. The seawater turnover timescale is constrained to be a few minutes based on the measured stable isotope values in the same sample. The residence time is especially sensitive to the range of $\delta^{13}C$ observed in the skeleton (Chen et al., 2018). The minor/trace element is removed from the ECF with an aragonite precipitation flux of F_{CaCO_3} and a distribution coefficient of $D_{Me} = \left(\frac{Me}{Ca}\right)_{arag} / \left(\frac{Me}{Ca}\right)_{ECF}$. The D_{Me} values for different elements are obtained from either aragonite precipitation experiments (Kinsman and Holland, 1969; Gaetani and Cohen, 2006) or empirical fits to coral data (Marriott et al., 2004; Reynaud et al., 2007; Montagna et al., 2014), and discussed in detail in the following sections. The term "*z*" represents the average thickness of the ECF. The geometry of the calcifying space in corals may be more complicated than sketched in Figure 10, and previous studies have estimated a range of values for the dimension of the ECF (Tambutté et al., 2007, 2011; Venn et al., 2011; Gagnon et al., 2012; Cai et al., 2016).

Here we picked a value of 10 μm for "*z*", which is on the higher end of previous observations (Venn et al., 2011; Cai et al., 2016) and suggested to be possible for deep-sea corals (Adkins et al., 2003; Gagnon et al., 2012). For Ca, there is an additional term that represents an alkalinity flux into the ECF by membrane transporters such as Ca-ATPase. The term "f_{Ca}" varies between 0 and 1 to account for the fact that not all alkalinity pumps are Ca transporters (Jokiel, 2013; Barott et al., 2015; Barron et al., 2018), and is important for the Ca budget and the incorporation of the minor/trace elements. As with the stable isotopes, the alkalinity pump is the primary perturbation in the model. Starting from seawater composition, the model is run toward steady state at a prescribed alkalinity pump rate with Matlab's ode15s solver.

In contrast to the metal cations, boron exists in seawater as $B(OH)_3$ and $B(OH)_4^-$, the proportions of which change as a function of pH. The incorporation mechanism of boron in carbonate minerals is a topic of active debate. Studies of inorganic and biogenic calcite have revealed different boron incorporation mechanisms (Hemming and Hanson, 1992; Klochko et al., 2009; Rollion-Bard et al., 2011; Rae et al., 2011; Branson et al., 2015; Noireaux et al., 2015; Uchikawa et al., 2015; Uchikawa et al., 2017; Farmer et al., 2019; Henehan et al., 2022). However, aragonite has been generally considered a relatively simple system dominated by $B(OH)_4^-$ incorporation, although debates remain as to which DIC species is substituted by $B(OH)_4^-$ (Mavromatis et al., 2015; Noireaux et al., 2015; Holcomb et al., 2016; Balan et al., 2016; Branson, 2018; Farmer et al., 2019). We test different boron incorporation rules for biogenic aragonite by comparing the deep-sea coral data to model outputs. The equation for boron in the model is formulated as:

$$\frac{d[B]}{dt} = \frac{1}{\tau_{sw}}([B]_{sw} - [B]) - D_B \frac{\chi_B [B]}{\chi_C [DIC]} \frac{F_{CaCO_3}}{z} \qquad (3)$$

In equation (3), χ_B is a fraction term that accounts for the boron species incorporated into the aragonite: for scenarios with sole borate incorporation, χ_B is the fraction of borate in total boron; and for the total boron incorporation scenario, χ_B equals 1. χ_C is the fraction of the DIC species being substituted by boron. The boron equation can be solved together with other elements to reveal tracer correlation patterns as a result of the biomineralization process.

Figure 11 shows the steady state responses of isotope and Me/Ca tracers to the prescribed alkalinity pump rates in our model. We see the depletion in $\delta^{18}O$ with increasing alkalinity pump rates (Figure 11a), interpreted as a stronger expression of the $CO_2(aq)$ hydration kinetic isotope effects at higher pH modulated by carbonic anhydrase activity (Chen et al., 2018). The $\delta^{18}O$ of the skeleton is insensitive to the fraction of Ca^{2+} pump (f_{Ca}), as it is dominantly controlled by the dynamics of the DIC system. As with $\delta^{18}O$, B/Ca is relatively insensitive to the f_{Ca} parameter (Figure 11c), as its incorporation also follows the DIC system. When we consider the total boron over DIC substitution rule as suggested in some calcite precipitation experiments (Uchikawa et al., 2015; Uchikawa et al., 2017; Farmer et al., 2019), skeletal B/Ca are mirror images of DIC changes with alkalinity pump rates (Figure 11b, c), since the removal of boron is limited by a very small D_B. The DIC changes mainly reflect the modulation of the cross-membrane carbon flux by carbonic anhydrase as previously discussed (Chen et al., 2018). In comparison, B/Ca increases with alkalinity pump rates when following the commonly suggested $B(OH)_4^-$ for HCO_3^- incorporation rule for aragonite (Hemming et al., 1995; Branson, 2018; Farmer et al., 2019). This is a result of both an increase in $B(OH)_4^-$ fraction in total boron and a decrease in HCO_3^- fraction in DIC at elevated pH.

In contrast, the metal cations are strongly influenced by the Ca^{2+} dynamics in the ECF, and therefore are sensitive to the f_{Ca} parameter. Figure 11b shows steady state $[Ca^{2+}]$ in the ECF at different f_{Ca} fractions. When f_{Ca} =1, there is limited change in [Ca^{2+}] due to a balance between Ca^{2+} pumped into the ECF and precipitated out as $CaCO_3$ in our steady-state model. When f_{Ca} decreases, a lower Ca^{2+} supply by active pumping causes lower ECF [Ca^{2+}] at higher pump rates and more Ca^{2+} contribution from seawater transport to balance the precipitation loss. In response, Mg/Ca and Li/Ca are perfect mirror images of [Ca^{2+}] (Figure 11d, e). Due to their low distribution coefficients, only a very small fraction of Mg and Li are removed by precipitation. As a result, the Mg/Ca and Li/Ca of the ECF and therefore the aragonite, are dominated by the Ca^{2+} dynamics, with lower [Ca^{2+}] corresponding to higher Mg/Ca and Li/Ca ratios. This is also the reason why Mg/Ca and Li/Ca have identical shapes in each model scenario (Figure 11d, e). On the contrary, Sr/Ca always decreases with alkalinity pump rates. This is a result of D_{Sr} being larger than 1 in aragonite, causing preferential Sr^{2+} removal relative to Ca^{2+} in the precipitation process regardless of the Ca^{2+}-pumping scenarios. With different sensitivities of the isotope and Me/Ca tracers to alkalinity pump rates and f_{Ca}, we can use model-data comparisons to learn about the relevant biomineralization processes underlying the vital effects.

4.2.2 Ion Pumping Effects

The observations of consistent tracer variability and correlations across measurement scales, especially in the aragonite fibers of the *D. dianthus* skeletons, strongly suggest control by a universal process in a dynamic biomineralization system. We have previously interpreted the stable isotope compositions of *D. dianthus* as a natural result of the internal pH elevation process modulated by carbonic anhydrase (Chen et al., 2018). It is reasonable to expect the incorporation of minor and trace elements to respond to the calcium and carbon dynamics in the ECF given the observed correlations between them and with $\delta^{18}O$. Previous studies have suggested Rayleigh distillation as the dominant control on the Me/Ca variability in corals (Sinclair and Risk, 2006; Gaetani and Cohen, 2006; Gagnon et al., 2007; Gaetani et al., 2011), as was first suggested in foraminifera calcification (Elderfield et al., 1996). We can further test this mechanism with the ECF carbonate chemistry independently constrained by the stable isotope measurements and our coral calcification model.

Figure 12 shows modeled tracer correlations in comparison with the data in coral 47407. The model results are generated with the same set of biological parameters as presented in Figure 11, assuming constant distribution coefficients for the minor and trace elements. Among the model cases with different fractions of Ca^{2+} in the alkalinity pump, we see that cases with low f_{Ca} best fit the tracer correlations and the range of variability in the data. As discussed in Section 3.5, f_{Ca} has different impacts on Li and Mg compared to Sr due to their different distribution coefficients. With distribution coefficients much smaller than 1, Li/Ca and Mg/Ca in the ECF (and therefore the skeleton) are dominantly controlled by [Ca^{2+}]. In order to generate a 2-fold change in Mg/Ca and Li/Ca in the coral skeleton, a 2-fold change in [Ca^{2+}] of the ECF is required if D is held constant. In contrast, with a distribution coefficient larger than 1, Sr^{2+} is preferentially removed relative to Ca^{2+} from the ECF into the aragonite skeleton, and a larger Ca^{2+} flux through the alkalinity pump causes more preferential removal of Sr^{2+} and thus a larger range in Sr/Ca ratios. Therefore, the relatively wide range in Mg/Ca and Li/Ca as well as the relatively narrow range in Sr/Ca observed in *D. dianthus* (Figure 3, 4) both require a small fraction of Ca^{2+} in the alkalinity pump (f_{Ca}). In addition, the negative correlation between Mg/Ca and $\delta^{18}O$ suggests that Mg is enriched relative to Ca as the alkalinity pump rate increases. Given a limited amount of Mg removal from the ECF by precipitation due to its small distribution coefficient, the observed Mg/Ca–$\delta^{18}O$ relation requires a decrease in [Ca^{2+}] with increasing alkalinity pump rates, further supporting the case for a low value of f_{Ca}.

While Ca-ATPase has been suggested to play an important role in the calcification process of surface corals (McConnaughey, 1989a; Al Horani et al., 2003; Zocolla et al., 2004), it may not be the most efficient way to facilitate precipitation. Given a 5:1 ratio of Ca^{2+} to DIC (and ~100:1 Ca^{2+}:CO_3^{2-} ratio) in seawater, the calcification process is more limited by DIC, while Ca^{2+} supply through seawater transport may be sufficient. Increasing the pH of the ECF through proton pumping, regardless of the involvement of Ca^{2+}, can increase the concentration of CO_3^{2-} by two mechanisms. First, the speciation of DIC shifts from HCO_3^- to CO_3^{2-} with increasing pH. In addition, higher pHs in the ECF lead to larger DIC concentrations due to the cross-membrane CO_2(aq) flux (as has been observed by Allison et al., 2014), until ~pK_{a2} when the [CO_2(aq)] gradient appoaches its maximum value. This extra carbon flux is enhanced by carbonic anhydrase because the enzyme efficiently converts new CO_2(aq) from outside the ECF to HCO_3^- (Chen et al., 2018). Both of these mechanisms relieve the lack of carbon relative to Ca and make Ca^{2+} pumping of lesser importance in the biomineralization process. A limited effect of Ca^{2+} pumping compared to total H^+ pumping has also been suggested in foraminifera (Vigier et al., 2015) as well as laboratory simulations of the biomineralization process (Zeebe and Sanyal, 2002), and is likely the calcification strategy used by deep-sea corals in an environment of relatively low aragonite saturation.

4.2.3 Possible Growth Rate Effects

Although the simple model with constant distribution coefficients can explain most tracer correlation features in the data with the low f_{Ca} case, the full range of Me/Ca variability would require f_{Ca} to be close to 0, and calls for pumps other than Ca-ATPase as the major source of alkalinity to the ECF in *D. dianthus*. In addition, microelectrode measurements of [Ca^{2+}] in the ECF of surface corals show slight increases relative to seawater (Al Horani et al., 2003), instead of a 2-fold decrease suggested by the our simple model (Figure 11b). While it is possible that deep-sea corals have different calcification dynamics, such a large discrepancy from surface corals would seem unlikely. Finally, in order to fit the Me/Ca ratios in the deep-sea coral data, we need specific distribution coefficients for Mg, Li and Sr. Among the three, only D_{Sr} is taken directly from inorganic aragonite precipitation experiments (Kinsman and Holland, 1969; Gaetani and Cohen, 2006). Both D_{Mg} and D_{Li} are derived from empirical fits to coral data (Reynaud et al., 2007; Montagna et al., 2014) and very different from the available constraints by inorganic experiments (Marriott et al., 2004; Gaetani and Cohen, 2006). These observations call for an additional mechanism not considered in our simple biomineralization model with constant distribution coefficients.

A likely candidate for the additional mechanism of tracer incorporation is the growth rate effect. In recent years, a number of carbonate precipitation experiments have been conducted to study the growth rate dependence of the incorporation of minor and trace elements (e.g. Gabitov et al., 2008; Tang et al., 2008; Mavromatis et al., 2013; Gabitov et al., 2014), as well as stable isotope fractionation (e.g. Tang et al., 2008; Gabitov et al., 2012; Gabitov, 2013; Watkins et al., 2013; Mavromatis et al., 2013). These experiments generally attempt to construct a sigmoid function of the distribution coefficients or fractionation factors with respect to $CaCO_3$ growth rates, with an equilibrium end member at low growth rates, a kinetic end member at high growth rates and a transition at intermediate growth rates (DePaolo, 2011). Theoretical frameworks for the growth rate dependence of the distribution coefficients and fractionation factors have been constructed based on the semi-empirical approach of a diffusion-related surface entrapment model (Watson, 2004), and a more mechanistic approach of an ion-by-ion growth model governed by energetics at the fluid-mineral interface (DePaolo, 2011; Nielsen et al., 2012, 2013; Watkins et al., 2013). We favor the ion-by-ion mechanism based on its successful application in our stable isotope model results (Chen et al., 2018). By applying the growth rate dependent oxygen isotope fractionation factors derived from the ion-by-ion growth model (Watkins et al., 2014), we generated an inorganic end member δ^{18}O and δ^{13}C composition that is consistent with the deep-sea coral data (Chen et al., 2018). Therefore it is reasonable to expect some growth rate dependence of the incorporation of minor and trace elements in the corals as well.

Application of the ion-by-ion model to Me/Ca ratios in the corals, however, is limited by the availability of experimental constraints. The number of aragonite precipitation experiments with minor and trace elements is much smaller than those for calcite, and very few have examined the growth rate dependence systematically (Gaetani and Cohen, 2006; Gabitov et al., 2008; Mavromatis et al., 2018). Therefore, we use the model formulation proposed in DePaolo (2011), and try to constrain the sigmoid of distribution coefficients with the deep-sea coral data. The sigmoid can be modeled as:

$$D = \frac{D_f}{1 + \frac{R_b}{R_f}\left(\frac{D_f}{D_{eq}} - 1\right)} \quad (4)$$

In Equation (4), D_f and D_{eq} are the distribution coefficients for the kinetic and equilibrium end members respectively. The effective D varies between the two end members modulated by the ratio of backward and forward reaction rates (R_b/R_f). While the DePaolo (2011) model equated the forward and backward reactions to gross carbonate precipitation and dissolution, an updated version of the model interpreted the forward and backward reactions as the attachment and detachment frequencies of specific ions to the mineral surface, and can therefore be different for different elements (Zhang and Nancollas, 1998; Nielsen et al., 2013). As one of the few existing systematic aragonite precipitation experiments, Gaetani and Cohen (2006) noted that their experimentally measured distribution coefficients for inorganic aragonite precipitated from seawater may be kinetically controlled and very different from thermodynamic considerations. We use their experimentally derived as well as theoretically calculated (based on lattice strain theory by Blundy and Wood, 1994) D_{Mg} and D_{Sr} as the reference points for our model.

Figure 13 shows the growth rate dependence of D_{Mg} and D_{Sr} calculated from the deep-sea coral isotope and Me/Ca data, obtained by using our biomineralization model to esimate the Me/Ca ratios in the ECF at the moment of calcification. The growth rates, as well as [Ca^{2+}] and carbonate chemistry in the ECF, are derived by fitting the stable isotope data of each coral with the model parameters used in Chen et al. (2018). The isotope-based [Ca^{2+}] and carbonate chemistry then allows us to simulate the Me/Ca ratios in the ECF corresponding to specific growth rates at different f_{Ca}, and calculate the required distribution coefficients from the measured Me/Ca data in the coral skeleton and the modeled Me/Ca ratio in the ECF. We see that little growth rate dependence is required to fit the data for the f_{Ca}=0 case (Figure 13a, 13d). As discussed in Section 4.2, the Ca^{2+} dynamics alone can drive most of the observed range in Me/Ca with constant distribution coefficients at f_{Ca}=0 (Figure 11). At higher f_{Ca}, the calculated D_{Mg} and D_{Sr} start to show increases with growth rates (Figure 13b, c, e, f). As f_{Ca} increases in the alkalinity pump, the [Ca^{2+}] change in the ECF is more strongly buffered (Figure 13b), therefore requiring a stronger growth rate dependence of the distribution coefficients to drive the observed Me/Ca changes. This effect influences D_{Sr} more than D_{Mg}, as more Ca^{2+} pumping (higher f_{Ca}) increases the preferential removal of Sr^{2+} (as discussed in Section 4.2.2), lowers Sr/Ca in the ECF, and requires higher D_{Sr}

to match the observed Sr/Ca in the corals. If we take the seawater aragonite precipitation experiments by Gaetani and Cohen (2006) as a constraint on the kinetic end member (1.33 at 5°C as the upper limit for D_{Sr}), a sensitivity test with our model suggests that f_{Ca} cannot exceed 0.1, which corresponds to limited Ca^{2+} pumping with a relatively weak growth rate dependence.

To further evaluate the growth rate effects in cation incorporation, it is instructive to compare the deep-sea coral data to inorganic experiments as well as other marine calcifying organisms, especially those that make aragonite. Recently it was discovered that the aragonitic benthic foraminifera *Hoeglundina elegans* shares the same Li/Mg–temperature relation with different coral species (Marchitto et al., 2018; Stewart et al., 2020). However, the Li/Ca, Mg/Ca and Sr/Ca ratios of *H.elegans* are lower than those of corals and closer to those of other calcitic foraminifera (Rosenthal et al., 2006; Bryan and Marchitto, 2008; Marchitto et al., 2018). A plausible explanation is a difference in growth rates between foraminifera and corals. Although it is difficult to constrain foraminifera growth rates, they are likely much lower than corals. A surface area normalized growth rate of planktonic foraminifera is estimated at 1×10^{-8} mol/m^2/s by Erez (2003), and that of benthic foraminifera in deep environments is likely even lower. We estimate the growth rates of *H.elegans* by assuming precipitation of aragonite from a medium similar to seawater with the same rate law as the deep-sea corals (Romanek et al., 2011; Chen et al., 2018). To account for the fact that some *H.elegans* were found in undersaturated seawater, we apply a 50% increase in the aragonite saturation state in their calcifying fluid relative to the ambient seawater, the minimum amount required for individuals living in the most undersaturated seawater to achieve supersaturation. The growth rates we obtain for *H.elegans* are in the range of 10^{-10}–10^{-9} mol/m^2/s, which are likely on the low end of possible growth rates given our conservative assumptions. When compared to corals, the relatively low growth rates of *H.elegans* may account for its low Me/Ca ratios (Figure 13). In fact, D_{Mg} and D_{Sr} of *H.elegans* are close to the thermodynamic values estimated by Gaetani and Cohen (2006) for aragonite based on the lattice strain theory (Blundy and Wood, 1994), while deep-sea corals have higher distribution coefficients (Figure 13). It is also noted that D_{Sr} obtained in seawater aragonite experiments by Zhong and Mucci (1989) fall between deep-sea corals and *H.elegans* with intermediate growth rates (Figure 13d). D_{Mg} values from experiments by Gabitov et al. (2008), in contrast, are significantly lower than other inorganic and biogenic carbonates (Figure 13a), likely due to the their specific experimental setup and very different Mg/Ca ratios in these experiments from seawater.

Although there is significant scatter in the compiled aragonite data, it is possible to derive the growth rate sigmoids for D_{Mg} and D_{Sr} in aragonite with Equation (4) at different backward reaction rates (R_b) as a sensitivity study. The sigmoid curves in Figure 13 show that the R_b values required for Mg and Sr are on the order of 10^{-7} and 10^{-10} mol/m^2/s respectively. The R_b for Sr is similar to aragonite dissolution rates measured in seawater near saturation (Dong et al., 2019), suggesting similar behavior of Sr and Ca in terms of attachment to and detachment from the mineral surface. The much higher R_b for Mg suggests higher detachment rates relative to attachment rates to the mineral surface, as incorporation of Mg in the aragonite lattice is thermodynamically unfavorable (Berner, 1975; Sun et al., 2015). The different growth rate sensitivities for Mg and Sr can therefore explain the relatively large difference in Sr/Ca between corals and *H.elegans*, as opposed to similar Mg/Ca values for the two different aragonite producers. Although these preliminary results suggest the possibility of a common mechanism for cation incorporation in inorganic and biogenic aragonite, we caution that the growth rate dependence derived here for aragonite has many uncertainties, and needs to be tested with more systematic inorganic aragonite precipitation experiments and more rigorous surface speciation models in the future. Meanwhile, we cannot rule out the possibility that the foraminifera calcification process is completely different from corals in terms of the biological controls and chemical flux balance, which we cannot account for in our simplified calculations.

4.2.4 Boron Incorporation Mechanism in Corals

While the metal cations are mainly controlled by the Ca^{2+} dynamics in the ECF, likely with an influence from growth rates, boron incorporation in carbonates follows the DIC system. However, the strong correlations between B/Ca, Mg/Ca and $\delta^{18}O$ in deep-sea corals, especially in the fibrous aragonite, suggests close coupling between calcium and carbon dynamics during the biomineralization process. To our knowledge, few studies have reported such strong correlations between boron and other elements for a coral species (Sinclair, 2005; Stewart et al., 2016; Wu et al., 2017). Through the negative Mg/Ca–$\delta^{18}O$ correlation, we have established how Mg can be enriched with increasing alkalinity pump rates. Therefore, a positive B/Ca–Mg/Ca correlation suggests B is also enriched as the alkalinity pump increases. By comparing model simulations to the data, we can test different boron incorporation mechanisms in the deep-sea corals.

Figure 14 shows the B/Ca–Mg/Ca correlation from SIMS measurements compared to model outputs of different boron partition rules. We consider both total boron and $B(OH)_4^-$ in the numerator of D_B, and DIC, HCO_3^-, and CO_3^{2-} in the denominator of D_B. We see that in order to get a positive B/Ca–Mg/Ca correlation (i.e. the left limb of the Mg/Ca–B/Ca "arch" seen in fibrous aragonite), $B(OH)_4^-$ has to be the species that gets incorporated (Figure 14a). Since the distribution coefficient of boron is much smaller than 1, the total boron in the ECF is minimally impacted by precipitation. Therefore the predicted B/Ca ratio would be controlled by the DIC dynamics if a distribution coefficient based on total boron is considered, just like Mg and Li are controlled by the Ca dynamics. Due to the catalytic effect of carbonic anhydrase, the DIC in the ECF is elevated above ambient seawater from the cross-membrane CO_2(aq) flux over a large range of alkalinity pump rates (Figure 11b, Chen et al., 2018). As a result, when total boron is incorporated, B/Ca would first decrease at elevated DIC (or HCO_3^-), and then increase after the precipitation rate is high enough to remove the extra DIC from the ECF (Figure 11c, 14b). This is the opposite of the pattern we observe at all scales in our modern deep-sea corals. In the case of total boron and $[CO_3^{2-}]$, B/Ca keeps decreasing because $[CO_3^{2-}]$ keeps increasing at elevated pump rates and higher pH (Figure 14b). In contrast, when only $B(OH)_4^-$ is incorporated, the increase in $B(OH)_4^-$ fraction at higher pH can outcompete the DIC increase and make B/Ca increase with Mg/Ca. However, when DIC or HCO_3^- is substituted by $B(OH)_4^-$, the predicted B/Ca increase is too rapid compared to the data (Figure 14a). In order to balance the B/Ca increase, the substituted species (the denominator in the boron partition rule) has to increase more rapidly than DIC and HCO_3^-, leaving CO_3^{2-} as the only candidate. However, since pK_{a2} (9.3 at 5°C) of the DIC system is higher than pK_B (8.8 at 5°C) of the boron system, CO_3^{2-} increases more rapidly than $B(OH)_4^-$ in the pH range of the ECF, causing a decrease in B/Ca at higher Mg/Ca when a $[B(OH)_4^-]/[CO_3^{2-}]$ rule is used (Figure 14a). The best agreement between the model and the range and relationships of the B/Ca and Mg/Ca data from the fibrous aragonite of the corals is found when the partition rule of $[B(OH)_4^-]/[CO_3^{2-}]^{0.5}$ is used (Figure 14a), as the square root term modulates the magnitude of $[CO_3^{2-}]$ change.

For boron incorporation in aragonite, it has generally been suggested by theory and observations that $B(OH)_4^-$ is the dominant species incorporated (Klochko et al., 2009; Noireaux et al., 2015; Holcomb et al., 2016; Balan et al., 2016; Branson, 2018; Farmer et al., 2019; Henehan et al., 2022). Our deep-sea coral data is consistent with this idea, providing support to the boron isotope proxy in *D. dianthus* based on the assumption of exclusive $B(OH)_4^-$ incorporation (Anagnostou et al., 2012; McCulloch et al., 2012; Stewart et al., 2016; Rae et al., 2018). The $[B(OH)_4^-]/[CO_3^{2-}]^{0.5}$ partition rule that best fits our Mg/Ca–B/Ca data in fibrous aragonite, though, has received less attention. The rule was proposed by Holcomb et al. (2016) based on a charge balanced exchange reaction, in which a $B(OH)_4^-$ only substitutes for half the charge of CO_3^{2-}, and the square root power comes from the CO_3^{2-} stoichiometric coefficient of the exchange reaction. Although the physical basis of such an exchange reaction is debatable, Holcomb et al. (2016) found that this rule explains most of the variance in their inorganic aragonite experiments. An equally good rule in Holcomb et al. (2016) that collapses the variance in their data is B_{total}/DIC, but we do not find it favorable for the deep-sea coral data. In addition, the D_B value estimated from the deep-sea coral data with the $[B(OH)_4^-]/[CO_3^{2-}]^{0.5}$ rule is within the range obtained from the inorganic precipitation experiments by Holcomb et al. (2016). It is important to understand the underlying physicochemical basis of this partition rule that applies to both corals and inorganic aragonite, and a detailed surface speciation model for boron in aragonite will be helpful. The surface speciation for boron in aragonite and calcite is likely very different (Branson, 2018; Farmer et al., 2019; Henehan et al., 2022), and it is unclear whether there is a significant growth rate effect on boron in aragonite. The increase in D_B with growth rate in calcite has been attributed to increased incorporation of $B(OH)_3$ at higher growth rates (Farmer et al., 2019), which is probably of lesser importance in aragonite. In fact, using a constant D_B already explains most of the B/Ca range in *D. dianthus*. The only exception is the COCs (i.e. the right limb of the Mg/Ca–B/Ca "arch"). The current biomineralization model based on known physicochemical rules cannot predict the low B/Ca in the COCs with the same rule as the aragonite fibers. The only model that reaches the measured COC composition is with the $[B(OH)_4^-]/[CO_3^{2-}]$ rule (Figure 14a). It is possible that a drastic change in growth conditions and surface energetics between COCs and aragonite fibers can cause a change in the apparent boron incorporation rule. It is also possible that the COCs formed from a different calcification mechanism such as amorphous $CaCO_3$ (ACC) precursors, as has been suggested in different calcifying organisms (Jacob et al., 2008; Rollion-Bard et al., 2010; Mass et al., 2017; Sun et al., 2020). Finally, we note that boric acid diffusion has recently been suggested to influence the $\delta^{11}B$ proxy in corals (Gagnon et al., 2021). We do not find the $B(OH)_3$ diffusion process can significantly alter the Mg/Ca–B/Ca correlation patterns in our model within a reasonable range of membrane $B(OH)_3$ diffusivities. In contrast, $B(OH)_3$ diffusion could influence the $\delta^{11}B$ of the coral skeletons more strongly by altering the $\delta^{11}B$ of total boron in the ECF.

4.2.5 Influence of Growth Environment on Coral Calcification

In the discussion above, we have focused on the spatially coherent tracer correlations in individual corals, and how they can be explained in the framework of a biomineralization model that considers the important fluxes in the calcification process. However, the calcification process is also expected to be sensitive to a coral's growth environment, as alluded to in the range of tracer variability in individual corals (Figures 2, 4, 8, 9). Numerous studies have shown the impact of ocean acidification and changes in the ambient saturation state on the growth of surface corals (e.g. Langdon et al., 2000; Cohen et al., 2009; Venn et al., 2013; Mollica et al., 2018), which is also reflected in the incorporation of minor and trace elements (Cohen et al., 2009; Gagnon et al., 2013). With a growth environment that is right around aragonite saturation, deep-sea corals provide a natural experiment to study the interaction between the ambient saturation state and the biomineralization process.

From the stable isotope results in *D. dianthus*, we see that corals from undersaturated seawater have a narrower range in $\delta^{13}C$ and $\delta^{18}O$ that is biased toward more enriched values (Figure 2). This is also reflected in the range of Mg/Ca variability, with corals from undersaturated seawater having a narrower range and lower mean values (Figure 9). In light of our biomineralization model, this suggests a limited amount of alkalinity pumping under the stress of ambient undersaturation. Figure 15 shows histograms of model-derived ECF pHs of four *D. dianthus* individuals with a relatively large number (N>25) of $\delta^{18}O$ measurements (this study and Adkins et al., 2003). We see that corals from undersaturated seawater (84820 and Titan) mostly have a pH upper limit of 9, while corals from supersaturated seawater (47407 and 78459) have a fraction of data points that are above pH 9. This difference suggests that the corals may only exert high alkalinity pump rates that take the ECF pH up to pK_{a2} in the fibrous aragonite (and beyond pK_{a2} in the COCs) of the carbonate system (~9.3 at 5°C) in a favorable growth condition of ambient supersaturation. Stress from ambient undersaturation may limit the amount of alkalinity pumping the corals utilize to make their skeleton and puts a lower threshold on the ECF pH than pK_{a2}, which has also been suggested for ocean acidification studies of surface corals (Gagnon et al., 2013; Venn et al., 2013). It is also noted that the minimum pH in the ECF is lower for corals from the thermocline (~8.3, Figure 15a) compared to those from below 2000m depth (~8.5, Figure 15b). Corals seem to need to achieve higher pH values in their ECF before precipitation can start when they grow at greater depths. This threshold pH is likely influenced by the effects of low temperature and high pressure on the aragonite saturation state (Ω_A) in the deep ocean. Indeed, through our model, we find that the threshold Ω_A in the ECF corresponding to the threshold pH is higher for the deep water corals (Ω_A=5.7) compared to the thermocline ones (Ω_A=3.6), after accounting for the temperature and pressure effects on aragonite solubility. We suspect that this is related to a pressure-dependent kinetic effect on aragonite precipitation in the deep ocean, in addition to the thermodynamic control on Ω_A. A pressure dependence on calcite dissolution kinetics has been experimentally observed, where raising the pressure by 700 dbar increases the dissolution rates of calcite by a factor of 2–4 compared to ambient pressure at the same saturation state (Dong et al., 2018). A similar pressure-related kinetic effect on precipitation may exist, as our model also predicts a minimum precipitation rate corresponding to the threshold pH in deep-water corals to be approximately twice as much as their thermocline counterparts. This is an interesting observation that warrants more robust experimental exploration. Finally, we also note that despite the differences in the range of ECF pH achieved in corals from supersaturated and undersaturated seawater, the differences in ECF pH corresponding to the mean $\delta^{18}O$ of each coral is very small (dashed lines in Figure 15). This is a result of the larger fractions of data points in the low to medium pH range for each coral that correspond to the fibrous aragonite in the skeletons. The small difference in mean ECF pH may explain the relatively low sensitivity of the $\delta^{11}B$–pH proxy ($\delta^{11}B_{coral}$–$\delta^{11}B_{borate}$ slopes much shallower than 1:1) in bulk deep-sea coral calibrations (Anagnostou et al., 2012; McCulloch et al., 2012; Stewart et al., 2016; Rae et al., 2018), while also allowing the bulk $\delta^{11}B$ values to retain a signal of external seawater pH despite the range of pHs experienced in the ECF.

In addition to alkalinity pump rates, it should be pointed out that there are other parameters in our model that can be changed for individual corals, including the seawater turnover rate and the f_{Ca} parameter. A natural response to ambient undersaturation for the corals would be to slow down the turnover rates of the corrosive seawater (increase τ_{sw}), and increase f_{Ca} through the pump to make up for the reduced Ca^{2+} supply from seawater. Such a response would make the ECF a more closed system and increase the pH at low pump rates (Chen et al., 2018; Chen et al., 2021), and change the associated Me/Ca variability. An example of such a case is coral Gaia from deep waters off of Tasmania, which has lower Me/Ca ratios than the other corals in our dataset (Figure 3, 4). An increase in f_{Ca} would limit the Mg enrichment and strengthen the Sr depletion effect (Figure 11e, f), while a slower growth rate may have also played a role in its lower Me/Ca values (Figure 13). Such a change in calcification strategy and its impact on tracers can have important implications for tracer-environment calibrations with bulk samples.

5. Synthesis

We have observed spatially coherent isotope and Me/Ca variability in the model deep-sea coral species *D. dianthus* that span a range of scales from a few microns to bulk samples. The coherent isotope and Me/Ca correlations in the fibrous aragonite can be systematically explained by a biomineralization model that simulates the internal pH-elevation process in the ECF of the corals. In response to the pH elevation, there is a depletion in $\delta^{13}C$, $\delta^{18}O$ and Sr/Ca, coupled to enrichments in Li/Ca, Mg/Ca and B/Ca, resulting in the observed correlation patterns. The correlations in the fibrous aragonite break down in the COCs for most of the tracers, suggesting the possibility of a different biomineralization mechanism in this skeletal texture.

The observed tracer variability and correlations in the fibrous aragonite of *D. dianthus* suggest control by an alkalinity pump with a low fraction of calcium ion transporters. The growth rate dependence of the incorporation of minor and trace elements may also play a role in determining the absolute Me/Ca ratios in deep-sea corals and explain the different Me/Ca ratios in different inorganic and biogenic aragonites. We also find that the positive Mg/Ca–B/Ca correlation in the fibrous aragonite supports the incorporation of $B(OH)_4^-$ in place of CO_3^{2-} in the coral skeleton.

Finally, we generally observe a narrower range in tracer variability and less extreme tracer values in corals from undersaturated seawater compared to those from supersaturated seawater, suggesting a change in the strength of the alkalinity pump in response to the ambient growth environment. This response may be the underlying mechanism of different environmental sensitivities of various carbonate chemistry proxies. By better understanding such mechanisms, we can potentially improve paleoceanographic tracers in deep-sea corals with a multi-proxy approach coupled with a quantitative, process-based biomineralization model in the future.

Acknowledgments

We thank Jessica Crumpton-Banks, Jared Marske and Grecia Ames for assistance in the lab. We would also like to thank Joe Stewart and Russell Day for providing standards for the geochemical analyses. Claire Rollion-Bard and three anonymous reviewers provided constructive comments that helped improve the manuscript. This research received funding from NSF grant OCE-1737404 awarded to JFA and China Scholarship Council Ph.D. Scholarship 201508020007 awarded to SC. SC was additionally sponsored by NSFC grant 42103081 and Shanghai Sailing Program grant 21YF1419100. JWBR was supported by ERC Starting Grant 805246 OldCO2NewArchives.

References

Adkins, J. F., Boyle, E. A., Curry, W. B., and Lutringer, A. (2003). Stable isotopes in deep-sea corals and a new mechanism for "vital effects." *Geochimica et Cosmochimica Acta*, *67*(6), 1129–1143.

Adkins, Jess F., Cheng, H., Boyle, E. A., Druffel, E. R. M., and Edwards, R. L. (1998). Deep-Sea Coral Evidence for Rapid Change in Ventilation of the Deep North Atlantic 15,400 Years Ago. *Science*, *280*(5364), 725–728.

Al-Horani, F. A., Al-Moghrabi, S. M., and de Beer, D. (2003). The mechanism of calcification and its relation to photosynthesis and respiration in the scleractinian coral *Galaxea fascicularis*. *Marine Biology*, *142*(3), 419–426.

Allison, N., Cohen, I., Finch, A. A., Erez, J., and Tudhope, A. W. (2014). Corals concentrate dissolved inorganic carbon to facilitate calcification. *Nature Communications*, *5*, 5741.

Anagnostou, E., Huang, K.-F., You, C.-F., Sikes, E. L., and Sherrell, R. M. (2012). Evaluation of boron isotope ratio as a pH proxy in the deep sea coral *Desmophyllum dianthus*: Evidence of physiological pH adjustment. *Earth and Planetary Science Letters*, *349–350*, 251–260.

Balan, E., Pietrucci, F., Gervais, C., Blanchard, M., Schott, J., and Gaillardet, J. (2016). First-principles study of boron speciation in calcite and aragonite. *Geochimica et Cosmochimica Acta*, *193*, 119–131.

Barott, K. L., Perez, S. O., Linsmayer, L. B., and Tresguerres, M. (2015). Differential localization of ion transporters suggests distinct cellular mechanisms for calcification and photosynthesis between two coral species. *American Journal of Physiology-Regulatory, Integrative and Comparative Physiology*, *309*(3), R235–R246.

Barron, M. E., Thies, A. B., Espinoza, J. A., Barott, K. L., Hamdoun, A., and Tresguerres, M. (2018). A vesicular Na^+/Ca^{2+} exchanger in coral calcifying cells. *PLOS ONE*, *13*(10), e0205367.

Berner, R. A. (1975). The role of magnesium in the crystal growth of calcite and aragonite from sea water. *Geochimica et Cosmochimica Acta*, *39*(4), 489–504.

Blamart, D., Rollion-Bard, C., Cuif, J.-P., Juillet-Leclerc, A., Lutringer, A., van Weering, T. C. E., and Henriet, J.-P. (2005). C and O isotopes in a deep-sea coral (Lophelia pertusa) related to skeletal microstructure. In A. Freiwald and J. M. Roberts (Eds.), *Cold-Water Corals and Ecosystems* (pp. 1005–1020). Springer Berlin Heidelberg.

Blundy, J., and Wood, B. (1994). Prediction of crystal–melt partition coefficients from elastic moduli. *Nature*, *372*(6505), 452–454.

Bonneau, L., Colin, C., Pons-Branchu, E., Mienis, F., Tisnérat-Laborde, N., Blamart, D., Elliot, M., Collart, T., Frank, N., Foliot, L., and Douville, E. (2018). Imprint of Holocene Climate Variability on Cold-Water Coral Reef Growth at the SW Rockall Trough Margin, NE Atlantic. *Geochemistry, Geophysics, Geosystems*, *19*(8), 2437–2452.

Branson, O. (2018). Boron Incorporation into Marine $CaCO_3$. In H. Marschall and G. Foster (Eds.), *Boron Isotopes: The Fifth Element* (pp. 71–105). Springer International Publishing.

Branson, O., Kaczmarek, K., Redfern, S. A. T., Misra, S., Langer, G., Tyliszczak, T., Bijma, J., and Elderfield, H. (2015). The coordination and distribution of B in foraminiferal calcite. *Earth and Planetary Science Letters*, *416*, 67–72.

Bryan, S. P., and Marchitto, T. M. (2008). Mg/Ca–temperature proxy in benthic foraminifera: New calibrations from the Florida Straits and a hypothesis regarding Mg/Li. *Paleoceanography*, *23*, PA2220.

Cai, W.-J., Ma, Y., Hopkinson, B. M., Grottoli, A. G., Warner, M. E., Ding, Q., Hu, X., Yuan, X., Schoepf, V., Xu, H., Han, C., Melman, T. F., Hoadley, K. D., Pettay, D. T., Matsui, Y., Baumann, J. H., Levas, S., Ying, Y., & Wang, Y. (2016). Microelectrode characterization of coral daytime interior pH and carbonate chemistry. *Nature Communications*, *7*(1), 1–8.

Case, D. H., Robinson, L. F., Auro, M. E., and Gagnon, A. C. (2010). Environmental and biological controls on Mg and Li in deep-sea scleractinian corals. *Earth and Planetary Science Letters*, *300*(3), 215–225.

Chen, S., Gagnon, A. C., and Adkins, J. F. (2018). Carbonic anhydrase, coral calcification and a new model of stable isotope vital effects. *Geochimica et Cosmochimica Acta*, *236*, 179–197.

Chen, S., Littley, E. F. M., Rae, J. W. B., Charles, C. D., and Adkins, J. F. (2021). Uranium Distribution and Incorporation Mechanism in Deep-Sea Corals: Implications for Seawater [CO_3^{2-}] Proxies. *Frontiers in Earth Science*, *9:641327*.

Cohen, A. L., McCorkle, D. C., Putron, S. de, Gaetani, G. A., and Rose, K. A. (2009). Morphological and compositional changes in the skeletons of new coral recruits reared in acidified seawater: Insights into the biomineralization response to ocean acidification. *Geochemistry, Geophysics, Geosystems*, *10*, Q07005.

de Nooijer, L. J., Toyofuku, T., and Kitazato, H. (2009). Foraminifera promote calcification by elevating their intracellular pH. *Proceedings of the National Academy of Sciences*, *106*(36), 15374–15378.

DePaolo, D. J. (2011). Surface kinetic model for isotopic and trace element fractionation during precipitation of calcite from aqueous solutions. *Geochimica et Cosmochimica Acta*, *75*(4), 1039–1056.

Dietzel, M., Gussone, N., and Eisenhauer, A. (2004). Co-precipitation of Sr^{2+} and Ba^{2+} with aragonite by membrane diffusion of CO_2 between 10 and 50 °C. *Chemical Geology*, *203*(1), 139–151.

Dong, S., Berelson, W. M., Rollins, N. E., Subhas, A. V., Naviaux, J. D., Celestian, A. J., Liu, X., Turaga, N., Kemnitz, N. J., Byrne, R. H., and Adkins, J. F. (2019). Aragonite dissolution kinetics and calcite/aragonite ratios in sinking and suspended particles in the North Pacific. *Earth and Planetary Science Letters*, *515*, 1–12.

Dong, S., Subhas, A. V., Rollins, N. E., Naviaux, J. D., Adkins, J. F., and Berelson, W. M. (2018). A kinetic pressure effect on calcite dissolution in seawater. *Geochimica et Cosmochimica Acta*, *238*, 411–423.

Elderfield, H., Bertram, C. J., and Erez, J. (1996). A biomineralization model for the incorporation of trace elements into foraminiferal calcium carbonate. *Earth and Planetary Science Letters*, *142*(3), 409–423.

Elliot, M., Colin, C., Douarin, M., Pons-Branchu, E., Tisnérat-Laborde, N., Schmidt, F., Michel, E., Dubois-Dauphin, Q., Dapoigny, A., Foliot, L., Miska, S., Thil, F., Long, D., and Douville, E. (2019). Onset and demise of coral reefs, relationship with regional ocean circulation on the Wyville Thomson Ridge. *Marine Geology*, *416*, 105969.

Erez, J. (2003). The Source of Ions for Biomineralization in Foraminifera and Their Implications for Paleoceanographic Proxies. *Reviews in Mineralogy and Geochemistry*, *54*(1), 115–149.

Farmer, J. R., Branson, O., Uchikawa, J., Penman, D. E., Hönisch, B., and Zeebe, R. E. (2019). Boric acid and borate incorporation in inorganic calcite inferred from B/Ca, boron isotopes and surface kinetic modeling. *Geochimica et Cosmochimica Acta*, *244*, 229–247.

Frank, N., Paterne, M., Ayliffe, L., van Weering, T., Henriet, J.-P., and Blamart, D. (2004). Eastern North Atlantic deep-sea corals: Tracing upper intermediate water $\Delta^{14}C$ during the Holocene. *Earth and Planetary Science Letters*, *219*(3), 297–309.

Gabitov, R. I., Gaetani, G. A., Watson, E. B., Cohen, A. L., and Ehrlich, H. L. (2008). Experimental determination of growth rate effect on U^{6+} and Mg^{2+} partitioning between aragonite and fluid at elevated U^{6+} concentration. *Geochimica et Cosmochimica Acta*, *72*(16), 4058–4068.

Gabitov, R. I., Gagnon, A. C., Guan, Y., Eiler, J. M., and Adkins, J. F. (2013). Accurate Mg/Ca, Sr/Ca, and Ba/Ca ratio measurements in carbonates by SIMS and NanoSIMS and an assessment of heterogeneity in common calcium carbonate standards. *Chemical Geology*, *356*, 94–108.

Gabitov, Rinat I. (2013). Growth-rate induced disequilibrium of oxygen isotopes in aragonite: An in situ study. *Chemical Geology*, *351*, 268–275.

Gabitov, Rinat I., Rollion-Bard, C., Tripati, A., and Sadekov, A. (2014). In situ study of boron partitioning between calcite and fluid at different crystal growth rates. *Geochimica et Cosmochimica Acta*, *137*, 81–92.

Gabitov, Rinat I., Watson, E. B., and Sadekov, A. (2012). Oxygen isotope fractionation between calcite and fluid as a function of growth rate and temperature: An in situ study. *Chemical Geology*, *306–307*, 92–102.

Gaetani, G. A., and Cohen, A. L. (2006). Element partitioning during precipitation of aragonite from seawater: A framework for understanding paleoproxies. *Geochimica et Cosmochimica Acta*, *70*(18), 4617–4634.

Gaetani, G. A., Cohen, A. L., Wang, Z., and Crusius, J. (2011). Rayleigh-based, multi-element coral thermometry: A biomineralization approach to developing climate proxies. *Geochimica et Cosmochimica Acta*, *75*(7), 1920–1932.

Gagnon, A. C., Adkins, J. F., and Erez, J. (2012). Seawater transport during coral biomineralization. *Earth and Planetary Science Letters*, *329–330*, 150–161.

Gagnon, A. C., Adkins, J. F., Erez, J., Eiler, J. M., and Guan, Y. (2013). Sr/Ca sensitivity to aragonite saturation state in cultured subsamples from a single colony of coral: Mechanism of biomineralization during ocean acidification. *Geochimica et Cosmochimica Acta*, *105*, 240–254.

Gagnon, A. C., Adkins, J. F., Fernandez, D. P., and Robinson, L. F. (2007). Sr/Ca and Mg/Ca vital effects correlated with skeletal architecture in a scleractinian deep-sea coral and the role of Rayleigh fractionation. *Earth and Planetary Science Letters*, *261*(1), 280–295.

Gagnon, A. C., Gothmann, A. M., Branson, O., Rae, J. W. B., and Stewart, J. A. (2021). Controls on boron isotopes in a cold-water coral and the cost of resilience to ocean acidification. *Earth and Planetary Science Letters*, *554*, 116662.

Goldstein, S. J., Lea, D. W., Chakraborty, S., Kashgarian, M., and Murrell, M. T. (2001). Uranium-series and radiocarbon geochronology of deep-sea corals: Implications for Southern Ocean ventilation rates and the oceanic carbon cycle. *Earth and Planetary Science Letters*, *193*(1), 167–182.

Hathorne, E. C., Gagnon, A., Felis, T., Adkins, J., Asami, R., Boer, W., Caillon, N., Case, D., Cobb, K. M., Douville, E., deMenocal, P., Eisenhauer, A., Garbe-Schönberg, D., Geibert, W., Goldstein, S., Hughen, K., Inoue, M., Kawahata, H., Kölling, M., Cornec, F. L., Linsley, B. K., McGregor, H. V., Montagna, P., Nurhati, I. S., Quinn, T. M., Raddatz, J., Rebaubier, H., Robinson, L., Sadekov, A., Sherrell, R., Sinclair, D., Tudhope, A. W., Wei, G., Wong, H., Wu, H. C., and You, C.-F. (2013). Interlaboratory study for coral Sr/Ca and other element/Ca ratio measurements. *Geochemistry, Geophysics, Geosystems*, *14*, 3730–3750.

Hemming, N. G., and Hanson, G. N. (1992). Boron isotopic composition and concentration in modern marine carbonates. *Geochimica et Cosmochimica Acta*, *56*(1), 537–543.

Hemming, N. G., Reeder, R. J., and Hanson, G. N. (1995). Mineral-fluid partitioning and isotopic fractionation of boron in synthetic calcium carbonate. *Geochimica et Cosmochimica Acta*, *59*(2), 371–379.

Henehan, M. J., Klein Gebbinck, C. D., Wyman, J. V. B., Hain, M. P., Rae, J. W. B., Hönisch, B., Foster, G. L., & Kim, S.-T. (2022). No ion is an island: Multiple ions influence boron incorporation into CaCO3. *Geochimica et Cosmochimica Acta*, *318*, 510–530.

Hines, S. K. V., Eiler, J. M., Southon, J. R., and Adkins, J. F. (2019). Dynamic Intermediate Waters Across the Late Glacial Revealed by Paired Radiocarbon and Clumped Isotope Temperature Records. *Paleoceanography and Paleoclimatology*, *34*(7), 1074–1091.

Holcomb, M., DeCarlo, T. M., Gaetani, G. A., and McCulloch, M. (2016). Factors affecting B/Ca ratios in synthetic aragonite. *Chemical Geology*, *437*, 67–76.

Jacob, D. E., Soldati, A. L., Wirth, R., Huth, J., Wehrmeister, U., and Hofmeister, W. (2008). Nanostructure, composition and mechanisms of bivalve shell growth. *Geochimica et Cosmochimica Acta*, *72*(22), 5401–5415.

Jochum, K. P., Stoll, B., Herwig, K., Willbold, M., Hofmann, A. W., Amini, M., Aarburg, S., Abouchami, W., Hellebrand, E., Mocek, B., Raczek, I., Stracke, A., Alard, O., Bouman, C., Becker, S., Dücking, M., Brätz, H., Klemd, R., de Bruin, D., Canil, D., Cornell, D., de Hoog, C.-J., Dalpé, C., Danyushevsky, L., Eisenhauer, A., Gao, Y., Snow., J., Groschopf, N., Günther, D., Latkoczy, C., Guillong, M., Hauri, E. H., Höfer, H. E., Lahaye, Y., Horz, K., Jacob, D. E., Kasemann, S. A., Kent, A. J. R., Ludwig, T., Zack, T., Mason, P. R. D., Meixner, A., Rosner, M., Misawa, K., Nash, B. P., Pfänder, J., Premo, W. R., Sun, W. D., Tiepolo, M., Vannucci, R., Vennemann, T., Wayne, D., and Woodhead, J. D. (2006). MPI-DING reference glasses for in situ microanalysis: New reference values for element concentrations and isotope ratios. *Geochemistry, Geophysics, Geosystems, 7*, Q02008.

Jokiel, P. L. (2013). Coral reef calcification: Carbonate, bicarbonate and proton flux under conditions of increasing ocean acidification. *Proceedings of the Royal Society B: Biological Sciences*, *280*(1764).

Kinsman, D. J. J., and Holland, H. D. (1969). The co-precipitation of cations with $CaCO_3$—IV. The co-precipitation of Sr^{2+} with aragonite between 16° and 96°C. *Geochimica et Cosmochimica Acta*, *33*(1), 1–17.

Klochko, K., Cody, G. D., Tossell, J. A., Dera, P., and Kaufman, A. J. (2009). Re-evaluating boron speciation in biogenic calcite and aragonite using ^{11}B MAS NMR. *Geochimica et Cosmochimica Acta*, *73*(7), 1890–1900.

Langdon, C., Takahashi, T., Sweeney, C., Chipman, D., Goddard, J., Marubini, F., Aceves, H., Barnett, H., and Atkinson, M. J. (2000). Effect of calcium carbonate saturation state on the calcification rate of an experimental coral reef. *Global Biogeochemical Cycles*, *14*(2), 639–654.

Li, T., Robinson, L. F., Chen, T., Wang, X. T., Burke, A., Rae, J. W. B., Pegrum-Haram, A., Knowles, T. D. J., Li, G., Chen, J., Ng, H. C., Prokopenko, M., Rowland, G. H., Samperiz, A., Stewart, J. A., Southon, J., & Spooner, P. T. (2020). Rapid shifts in circulation and biogeochemistry of the Southern Ocean during deglacial carbon cycle events. *Science Advances*, *6*(42), eabb3807.

Marchitto, T. M., Bryan, S. P., Doss, W., McCulloch, M. T., and Montagna, P. (2018). A simple biomineralization model to explain Li, Mg, and Sr incorporation into aragonitic foraminifera and corals. *Earth and Planetary Science Letters*, *481*, 20–29.

Marriott, C. S., Henderson, G. M., Belshaw, N. S., and Tudhope, A. W. (2004). Temperature dependence of δ^7Li, δ^{44}Ca and Li/Ca during growth of calcium carbonate. *Earth and Planetary Science Letters*, *222*(2), 615–624.

Mass, T., Giuffre, A. J., Sun, C.-Y., Stifler, C. A., Frazier, M. J., Neder, M., Tamura, N., Stan, C. V., Marcus, M. A., and Gilbert, P. U. P. A. (2017). Amorphous calcium carbonate particles form coral skeletons. *Proceedings of the National Academy of Sciences*, *114*(37), E7670–E7678.

Mavromatis, V., Goetschl, K. E., Grengg, C., Konrad, F., Purgstaller, B., and Dietzel, M. (2018). Barium partitioning in calcite and aragonite as a function of growth rate. *Geochimica et Cosmochimica Acta*, *237*, 65–78.

Mavromatis, Vasileios, Gautier, Q., Bosc, O., and Schott, J. (2013). Kinetics of Mg partition and Mg stable isotope fractionation during its incorporation in calcite. *Geochimica et Cosmochimica Acta*, *114*, 188–203.

Mavromatis, V., Montouillout, V., Noireaux, J., Gaillardet, J., and Schott, J. (2015). Characterization of boron incorporation and speciation in calcite and aragonite from co-precipitation experiments under controlled pH, temperature and precipitation rate. *Geochimica et Cosmochimica Acta*, 150, 299–313. https://doi.org/10.1016/j.gca.2014.10.024

McConnaughey, T. (1989a). ^{13}C and ^{18}O isotopic disequilibrium in biological carbonates: I. Patterns. *Geochimica et Cosmochimica Acta*, *53*(1), 151–162.

McConnaughey, T. (1989b). ^{13}C and ^{18}O isotopic disequilibrium in biological carbonates: II. In vitro simulation of kinetic isotope effects. *Geochimica et Cosmochimica Acta*, *53*(1), 163–171.

McCulloch, M., Trotter, J., Montagna, P., Falter, J., Dunbar, R., Freiwald, A., Försterra, G., López Correa, M., Maier, C., Rüggeberg, A., and Taviani, M. (2012). Resilience of cold-water scleractinian corals to ocean acidification: Boron isotopic systematics of pH and saturation state up-regulation. *Geochimica et Cosmochimica Acta*, *87*, 21–34.

Mollica, N. R., Guo, W., Cohen, A. L., Huang, K.-F., Foster, G. L., Donald, H. K., and Solow, A. R. (2018). Ocean acidification affects coral growth by reducing skeletal density. *Proceedings of the National Academy of Sciences*, *115*(8), 1754–1759.

Montagna, P., McCulloch, M., Douville, E., López Correa, M., Trotter, J., Rodolfo-Metalpa, R., Dissard, D., Ferrier-Pagès, C., Frank, N., Freiwald, A., Goldstein, S., Mazzoli, C., Reynaud, S., Rüggeberg, A., Russo, S., and Taviani, M. (2014). Li/Mg systematics in scleractinian corals: Calibration of the thermometer. *Geochimica et Cosmochimica Acta*, *132*, 288–310.

Montero-Serrano, J.-C., Frank, N., Tisnérat-Laborde, N., Colin, C., Wu, C.-C., Lin, K., Shen, C.-C., Copard, K., Orejas, C., Gori, A., De Mol, L., Van Rooij, D., Reverdin, G., and Douville, E. (2013). Decadal changes in the mid-depth water mass dynamic of the Northeastern Atlantic margin (Bay of Biscay). *Earth and Planetary Science Letters*, *364*, 134–144.

Nielsen, L. C., De Yoreo, J. J., and DePaolo, D. J. (2013). General model for calcite growth kinetics in the presence of impurity ions. *Geochimica et Cosmochimica Acta*, *115*, 100–114.

Nielsen, L. C., DePaolo, D. J., and De Yoreo, J. J. (2012). Self-consistent ion-by-ion growth model for kinetic isotopic fractionation during calcite precipitation. *Geochimica et Cosmochimica Acta*, *86*, 166–181.

Noireaux, J., Mavromatis, V., Gaillardet, J., Schott, J., Montouillout, V., Louvat, P., Rollion-Bard, C., and Neuville, D. R. (2015). Crystallographic control on the boron isotope paleo-pH proxy. *Earth and Planetary Science Letters*, *430*, 398–407.

Polerecky, L., Adam, B., Milucka, J., Musat, N., Vagner, T., and Kuypers, M. M. M. (2012). Look@NanoSIMS--a tool for the analysis of NanoSIMS data in environmental microbiology. *Environmental Microbiology*, *14*(4), 1009–1023.

Rae, J. W. B., Burke, A., Robinson, L. F., Adkins, J. F., Chen, T., Cole, C., Greenop, R., Li, T., Littley, E. F. M., Nita, D. C., Stewart, J. A., and Taylor, B. J. (2018). CO_2 storage and release in the deep Southern Ocean on millennial to centennial timescales. *Nature*, *562*(7728), 569–573.

Rae, James W. B., Foster, G. L., Schmidt, D. N., and Elliott, T. (2011). Boron isotopes and B/Ca in benthic foraminifera: Proxies for the deep ocean carbonate system. *Earth and Planetary Science Letters*, *302*(3), 403–413.

Reynaud, S., Ferrier-Pagès, C., Meibom, A., Mostefaoui, S., Mortlock, R., Fairbanks, R., and Allemand, D. (2007). Light and temperature effects on Sr/Ca and Mg/Ca ratios in the scleractinian coral Acropora sp. *Geochimica et Cosmochimica Acta*, *71*(2), 354–362.

Robinson, L. F., Adkins, J. F., Fernandez, D. P., Burnett, D. S., Wang, S.-L., Gagnon, A. C., and Krakauer, N. (2006). Primary U distribution in scleractinian corals and its implications for U series dating. *Geochemistry, Geophysics, Geosystems*, *7*, Q05022.

Robinson, L. F., Adkins, J. F., Frank, N., Gagnon, A. C., Prouty, N. G., Brendan Roark, E., and de Flierdt, T. van. (2014). The geochemistry of deep-sea coral skeletons: A review of vital effects and applications for palaeoceanography. *Deep Sea Research Part II: Topical Studies in Oceanography*, *99*, 184–198.

Robinson, L. F., Adkins, J. F., Keigwin, L. D., Southon, J., Fernandez, D. P., Wang, S.-L., and Scheirer, D. S. (2005). Radiocarbon Variability in the Western North Atlantic During the Last Deglaciation. *Science*, *310*(5753), 1469–1473.

Rollion-Bard, C., and Blamart, D. (2015). Possible controls on Li, Na, and Mg incorporation into aragonite coral skeletons. *Chemical Geology*, *396*, 98–111.

Rollion-Bard, C., Blamart, D., Cuif, J.-P., and Dauphin, Y. (2010). In situ measurements of oxygen isotopic composition in deep-sea coral, Lophelia pertusa: Re-examination of the current geochemical models of biomineralization. *Geochimica et Cosmochimica Acta*, *74*(4), 1338–1349.

Rollion-Bard, C., Blamart, D., Trebosc, J., Tricot, G., Mussi, A., and Cuif, J.-P. (2011). Boron isotopes as pH proxy: A new look at boron speciation in deep-sea corals using 11B MAS NMR and EELS. *Geochimica et Cosmochimica Acta*, *75*(4), 1003–1012.

Rollion-Bard, C., Chaussidon, M., and France-Lanord, C. (2003). pH control on oxygen isotopic composition of symbiotic corals. *Earth and Planetary Science Letters*, *215*(1), 275–288.

Romanek, C. S., Morse, J. W., and Grossman, E. L. (2011). Aragonite Kinetics in Dilute Solutions. *Aquatic Geochemistry*, *17*(4), 339.

Rosenthal, Y., Lear, C. H., Oppo, D. W., and Linsley, B. K. (2006). Temperature and carbonate ion effects on Mg/Ca and Sr/Ca ratios in benthic foraminifera: Aragonitic species Hoeglundina elegans. *Paleoceanography*, *21*, PA1007.

Sinclair, D. J. (2005). Correlated trace element “vital effects” in tropical corals: A new geochemical tool for probing biomineralization. *Geochimica et Cosmochimica Acta*, *69*(13), 3265–3284.

Sinclair, D. J., and Risk, M. J. (2006). A numerical model of trace-element coprecipitation in a physicochemical calcification system: Application to coral biomineralization and trace-element 'vital effects.' *Geochimica et Cosmochimica Acta*, *70*(15), 3855–3868.

Smith, J. E., Risk, M. J., Schwarcz, H. P., and McConnaughey, T. A. (1997). Rapid climate change in the North Atlantic during the Younger Dryas recorded by deep-sea corals. *Nature*, *386*(6627), 818–820.

Smith, J. E., Schwarcz, H. P., and Risk, M. J. (2002). Patterns of isotopic disequilibria in azooxanthellate coral skeletons. *Hydrobiologia*, *471*(1), 111–115.

Stewart, J. A., Anagnostou, E., and Foster, G. L. (2016). An improved boron isotope pH proxy calibration for the deep-sea coral Desmophyllum dianthus through sub-sampling of fibrous aragonite. *Chemical Geology*, *447*, 148–160.

Stewart, J. A., Christopher, S. J., Kucklick, J. R., Bordier, L., Chalk, T. B., Dapoigny, A., Douville, E., Foster, G. L., Gray, W. R., Greenop, R., Gutjahr, M., Hemsing, F., Henehan, M. J., Holdship, P., Hsieh, Y.-T., Kolevica, A., Lin, Y.-P., Mawbey, E. M., Rae, J. W. B., … Day, R. D. (2021). NIST RM 8301 Boron Isotopes in Marine Carbonate (Simulated Coral and Foraminifera Solutions): Inter-laboratory δ^{11}B and Trace Element Ratio Value Assignment. *Geostandards and Geoanalytical Research*, *45*(1), 77–96.

Stewart, J. A., Robinson, L. F., Day, R. D., Strawson, I., Burke, A., Rae, J. W. B., Spooner, P. T., Samperiz, A., Etnoyer, P. J., Williams, B., Paytan, A., Leng, M. J., Häussermann, V., Wickes, L. N., Bratt, R., and Pryer, H. (2020). Refining trace metal temperature proxies in cold-water scleractinian and stylasterid corals. *Earth and Planetary Science Letters*, *545*, 116412.

Sun, C.-Y., Stifler, C. A., Chopdekar, R. V., Schmidt, C. A., Parida, G., Schoeppler, V., Fordyce, B. I., Brau, J. H., Mass, T., Tambutté, S., and Gilbert, P. U. P. A. (2020). From particle attachment to space-filling coral skeletons. *Proceedings of the National Academy of Sciences*, *117*(48), 30159–30170.

Sun, W., Jayaraman, S., Chen, W., Persson, K. A., & Ceder, G. (2015). Nucleation of metastable aragonite $CaCO_3$ in seawater. *Proceedings of the National Academy of Sciences*, *112*(11), 3199–3204.

Tambutté, E., Allemand, D., Zoccola, D., Meibom, A., Lotto, S., Caminiti, N., & Tambutté, S. (2007). Observations of the tissue-skeleton interface in the scleractinian coral Stylophora pistillata. *Coral Reefs*, *26*(3), 517–529.

Tambutté, S., Holcomb, M., Ferrier-Pagès, C., Reynaud, S., Tambutté, É., Zoccola, D., & Allemand, D. (2011). Coral biomineralization: From the gene to the environment. *Journal of Experimental Marine Biology and Ecology*, *408*(1), 58–78.

Tang, J., Dietzel, M., Böhm, F., Köhler, S. J., and Eisenhauer, A. (2008). Sr^{2+}/Ca^{2+} and 44Ca/40Ca fractionation during inorganic calcite formation: II. Ca isotopes. *Geochimica et Cosmochimica Acta*, *72*(15), 3733–3745.

Thiagarajan, N., Subhas, A. V., Southon, J. R., Eiler, J. M., and Adkins, J. F. (2014). Abrupt pre-Bølling–Allerød warming and circulation changes in the deep ocean. *Nature*, *511*(7507), 75–78.

Toyofuku, T., Matsuo, M. Y., de Nooijer, L. J., Nagai, Y., Kawada, S., Fujita, K., Reichart, G.-J., Nomaki, H., Tsuchiya, M., Sakaguchi, H., and Kitazato, H. (2017). Proton pumping accompanies calcification in foraminifera. *Nature Communications*, *8*, 14145.

Uchikawa, J., Harper, D. T., Penman, D. E., Zachos, J. C., and Zeebe, R. E. (2017). Influence of solution chemistry on the boron content in inorganic calcite grown in artificial seawater. *Geochimica et Cosmochimica Acta*, *218*, 291–307.

Uchikawa, J., Penman, D. E., Zachos, J. C., and Zeebe, R. E. (2015). Experimental evidence for kinetic effects on B/Ca in synthetic calcite: Implications for potential $B(OH)_4^-$ and $B(OH)_3$ incorporation. *Geochimica et Cosmochimica Acta*, *150*, 171–191.

Venn, A. A., Tambutté, E., Holcomb, M., Laurent, J., Allemand, D., and Tambutté, S. (2013). Impact of seawater acidification on pH at the tissue-skeleton interface and calcification in reef corals. *Proceedings of the National Academy of Sciences of the United States of America*, *110*(5), 1634–1639.

Venn, A., Tambutté, E., Holcomb, M., Allemand, D., and Tambutté, S. (2011). Live Tissue Imaging Shows Reef Corals Elevate pH under Their Calcifying Tissue Relative to Seawater. *PLOS ONE*, *6*(5), e20013.

Vigier, N., Rollion-Bard, C., Levenson, Y., and Erez, J. (2015). Lithium isotopes in foraminifera shells as a novel proxy for the ocean dissolved inorganic carbon (DIC). *Comptes Rendus Geoscience*, *347*(1), 43–51.

Wang, X. T., Sigman, D. M., Prokopenko, M. G., Adkins, J. F., Robinson, L. F., Hines, S. K., Chai, J., Studer, A. S., Martínez-García, A., Chen, T., and Haug, G. H. (2017). Deep-sea coral evidence for lower Southern Ocean surface nitrate concentrations during the last ice age. *Proceedings of the National Academy of Sciences*, *114*(13), 3352–3357.

Watkins, J. M., Hunt, J. D., Ryerson, F. J., and DePaolo, D. J. (2014). The influence of temperature, pH, and growth rate on the $\delta^{18}O$ composition of inorganically precipitated calcite. *Earth and Planetary Science Letters*, *404*, 332–343.

Watkins, J. M., Nielsen, L. C., Ryerson, F. J., and DePaolo, D. J. (2013). The influence of kinetics on the oxygen isotope composition of calcium carbonate. *Earth and Planetary Science Letters*, *375*, 349–360.

Watson, E. B. (2004). A conceptual model for near-surface kinetic controls on the trace-element and stable isotope composition of abiogenic calcite crystals. *Geochimica et Cosmochimica Acta*, *68*(7), 1473–1488.

Wilson, D. J., Struve, T., van de Flierdt, T., Chen, T., Li, T., Burke, A., and Robinson, L. F. (2020). Sea-ice control on deglacial lower cell circulation changes recorded by Drake Passage deep-sea corals. *Earth and Planetary Science Letters*, *544*, 116405.

Wu, H. C., Dissard, D., Le Cornec, F., Thil, F., Tribollet, A., Moya, A., and Douville, E. (2017). Primary Life Stage Boron Isotope and Trace Elements Incorporation in Aposymbiotic *Acropora millepora* Coral under Ocean Acidification and Warming. *Frontiers in Marine Science*, *4:129*.

Zeebe, R. E., and Rae, J. W. B. (2020). Equilibria, kinetics, and boron isotope partitioning in the aqueous boric acid–hydrofluoric acid system. *Chemical Geology*, *550*, 119693.

Zeebe, R. E., and Sanyal, A. (2002). Comparison of two potential strategies of planktonic foraminifera for house building: Mg^{2+} or H^+ removal? *Geochimica et Cosmochimica Acta*, *66*(7), 1159–1169.

Zhang, J., and Nancollas, G. H. (1998). Kink Density and Rate of Step Movement during Growth and Dissolution of anABCrystal in a Nonstoichiometric Solution. *Journal of Colloid and Interface Science*, *200*(1), 131–145.

Zhong, S., and Mucci, A. (1989). Calcite and aragonite precipitation from seawater solutions of various salinities: Precipitation rates and overgrowth compositions. *Chemical Geology*, *78*(3), 283–299.

Zoccola, D., Tambutté, E., Kulhanek, E., Puverel, S., Scimeca, J.-C., Allemand, D., and Tambutté, S. (2004). Molecular cloning and localization of a PMCA P-type calcium ATPase from the coral *Stylophora pistillata*. *Biochimica Et Biophysica Acta, 1663*(1–2), 117–126.

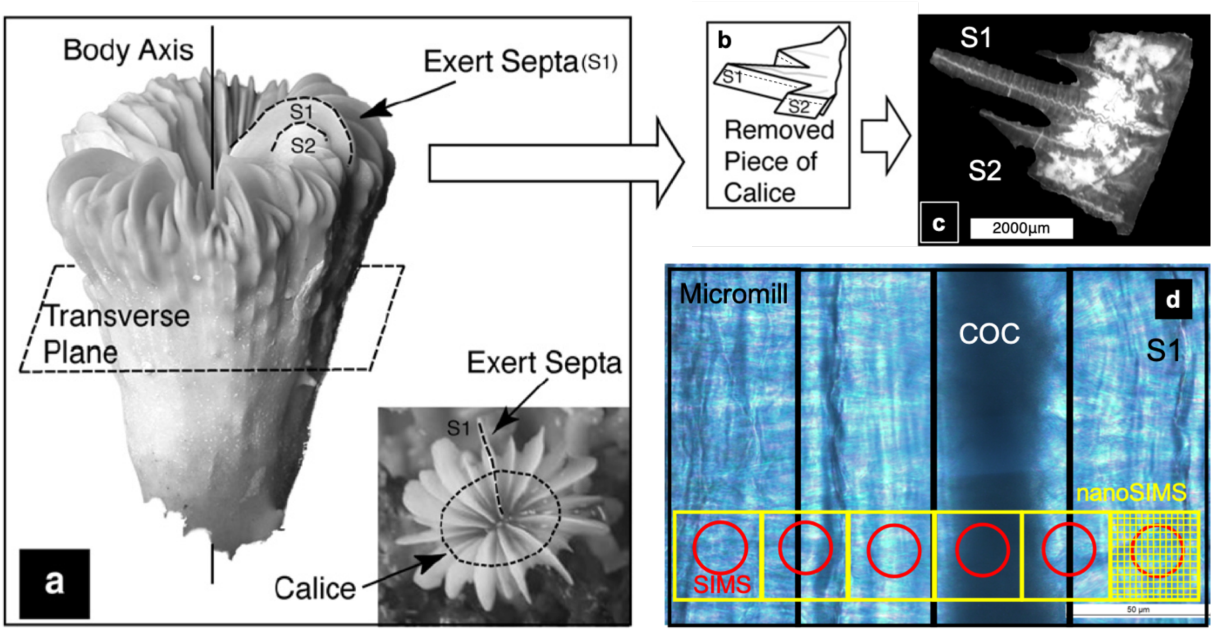

Figure 1 Schematic diagram of the sampling process. (a) The main panel shows the front view of a *D. dianthus* calice (~7 cm in height). The inset shows the top view of the calice along the transverse plane (~4 cm in diameter, Gagnon et al., 2007). (b) A thick slice of the calice is cut from the top view (5–10 mm in width, ~1 mm thick). The thick slice can be split into two thinner layers with a diamond saw blade, as illustrated by the dashed lines. The two thinner pieces can be polished and used for micromilling and SIMS/nanoSIMS analyses respectively. (c) A reflected light image of a thick section of *D. dianthus* taken with an Olympus SZ-CTV microscope. The two septa S1 and S2 both have a white COC band running through the middle, surrounded by dark aragonite fibers on each side. The theca is a mixture of COC-like white material and fibrous-aragonite-like dark material. (d) A transmitted light image of the S1 septum taken with a Leica DM2500P microscope. The COC shows up as the dark band in the middle. The fibrous aragonite shows needle-like patterns radiating from the COC. Micromilling typically samples the whole growth band along its orientation as shown by the black rectangles. The actual lengths of the micromilled bands are longer than those shown in this image. The SIMS O^- beam typically measures a spot 25–30 µm in size, as shown by the red circles. The nanoSIMS measurements sample a square region similar in size to a SIMS spot, and make a 512×512 pixel element map of the whole square. The rightmost yellow square with grid lines illustrates this mapping process but with much lower resolution than the actual measurements.

Table 1 Me/Ca measurements of Jcp-1 standard

Ratio	Calibration Standard	Li/Ca (µmol/mol)	B/Ca (µmol/mol)	Mg/Ca (mmol/mol)	Sr/Ca (mmol/mol)
Hathorne (2013)	Multiple Labs	6.185±0.107	459.6±22.7	4.199±0.065	8.838±0.042
Caltech uncleaned	8301C (N=15)	6.350±0.089	476.2±9.1	4.215±0.022	8.692±0.051
St Andrews uncleaned	BSGS/8301C (N=3)	6.003±0.282	428.3±3.5	4.199±0.054	8.743±0.033
St Andrews cleaned	BSGS/8301C (N=4)	4.709±0.147	357.6±12.5	3.168±0.193	8.723±0.023

Note: Errors for Caltech measurements are standard deviations (1 SD) of replicate measurements of different dilutions of a Jcp-1 solution made from fresh powder without chemical cleaning. The St Andrews measurement errors are 1 SD of replicate measurements of a single solution, and results for both cleaned and uncleaned powder are shown. The Hathorne et al. (2013) values are robust means and standard deviations (1σ) of an interlab calibration effort as originally reported.

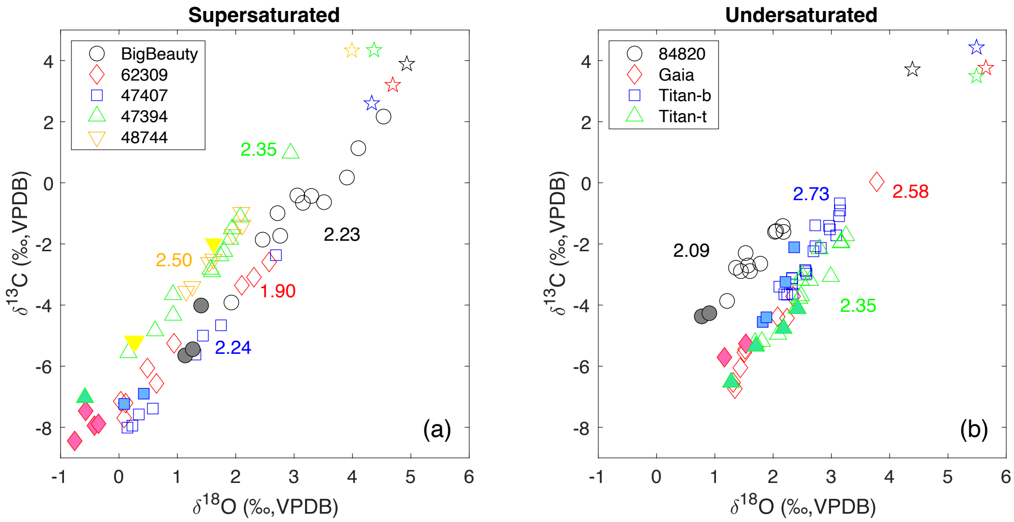

Figure 2 Stable isotope compositions of micromilled bands in *D. dianthus* individuals. Open symbols indicate aragonite fibers, and filled symbols indicate samples from regions containing COCs or COC-like structures from the same coral, though we note that given the sample sizes these likely contain a mix of both COC material and fibrous aragonite. Panel (a) shows corals from supersaturated seawater with respect to aragonite ($\Omega_A > 1$), while panel (b) shows corals from undersaturated seawater with respect to aragonite ($\Omega_A < 1$). The numbers show the least-squares $\delta^{18}O$–$\delta^{13}C$ slopes calculated from fibrous aragonite data points of the same color. The stars show the expected compositions of inorganic aragonite precipitated directly from the seawater each coral grew in (with corresponding symbol colors), following the model approach of Chen et al. (2018).

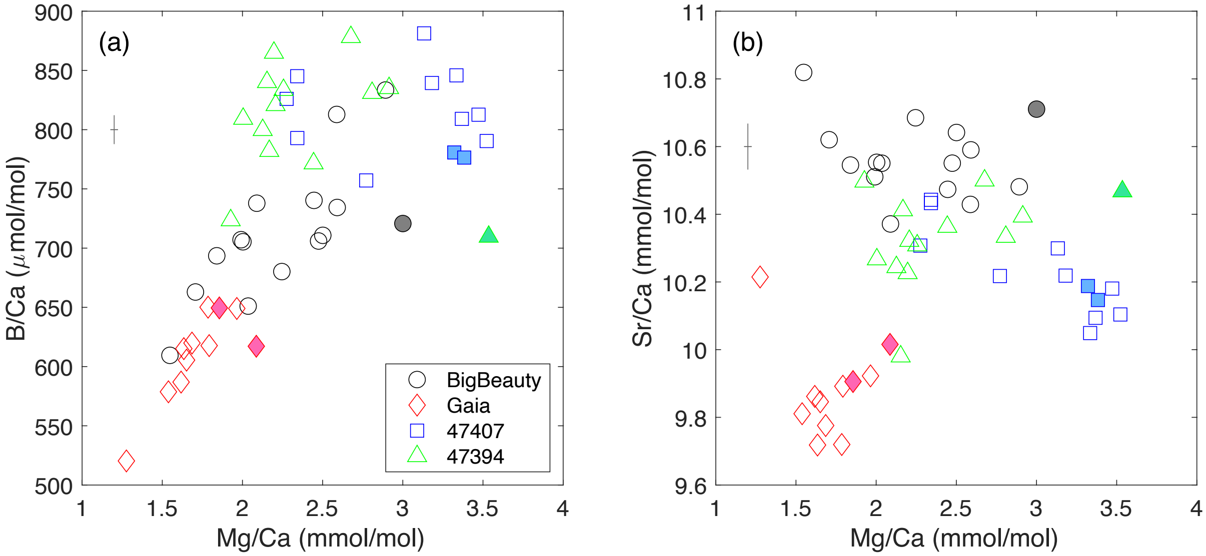

Figure 3 Correlations of Mg/Ca with (a) B/Ca and (b) Sr/Ca from micromilled samples in different *D. dianthus* individuals measured at Caltech. The open symbols represent aragonite fibers, while filled symbols represent COCs or COC-like structures, though we note that given the sampling size these likely contain a mix of both COC material and fibrous aragonite. The black crosses on the upper left corners in each panel mark average analytical uncertainties (2 SD) of the micromilled samples.

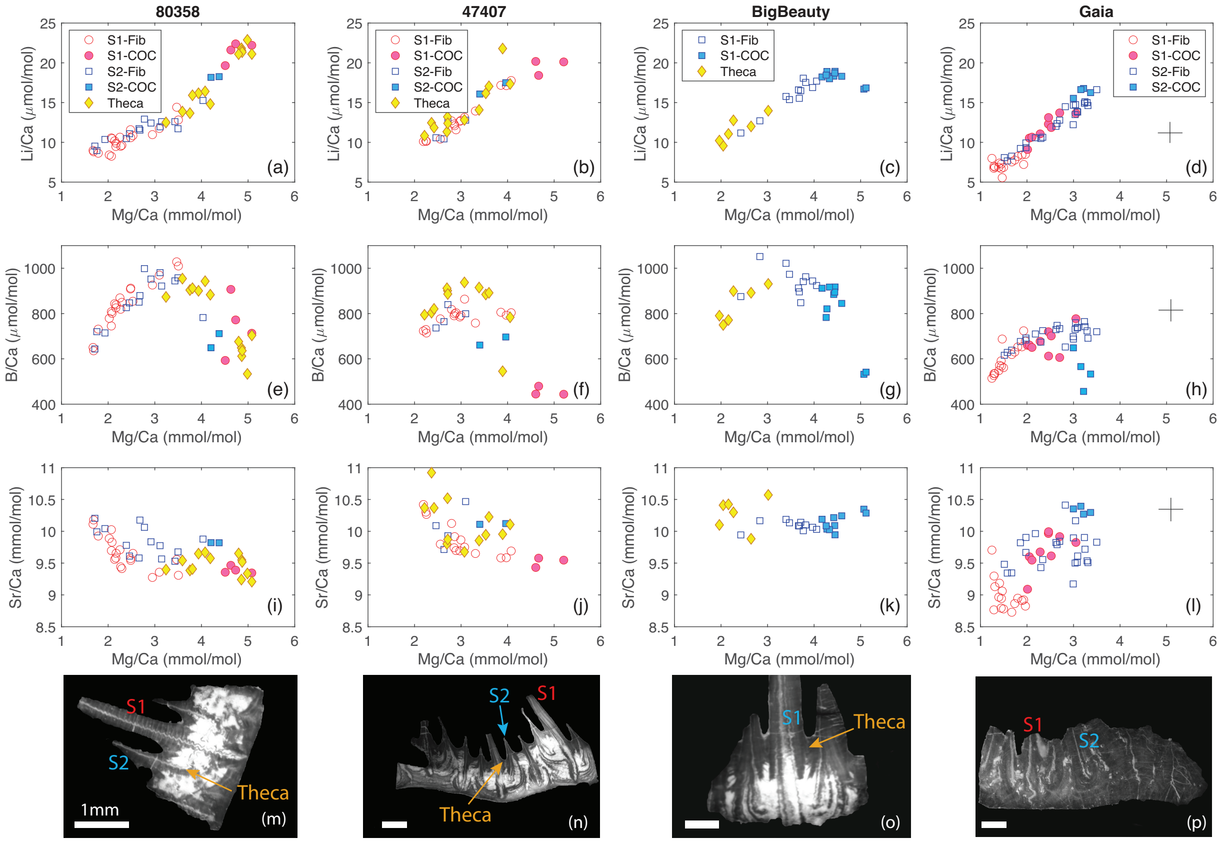

Figure 4 Me/Ca correlations measured by SIMS on four individual *D. dianthus*, with each column corresponding to one individual. Row 1 (a–d), row 2 (e–h) and row 3 (i–l) show Mg/Ca correlations with Li/Ca, B/Ca and Sr/Ca in each coral respectively. Red circles and blue squares represent spots from different septa (S1 and S2) of the same coral, with open symbols showing aragonite fibers and filled symbols showing COCs. Yellow diamonds represent spots from the theca regions of the corals. The bottom row (m–p) shows reflected light images of a thick section of each coral with locations of the SIMS data points. The white scale bars in each image correspond to 1 mm. For Gaia, the S2 data points come from the bottom of the septum very close to the theca. The black crosses in panels (d), (h) and (l) mark average analytical uncertainties (2 SD) of all the SIMS data points.

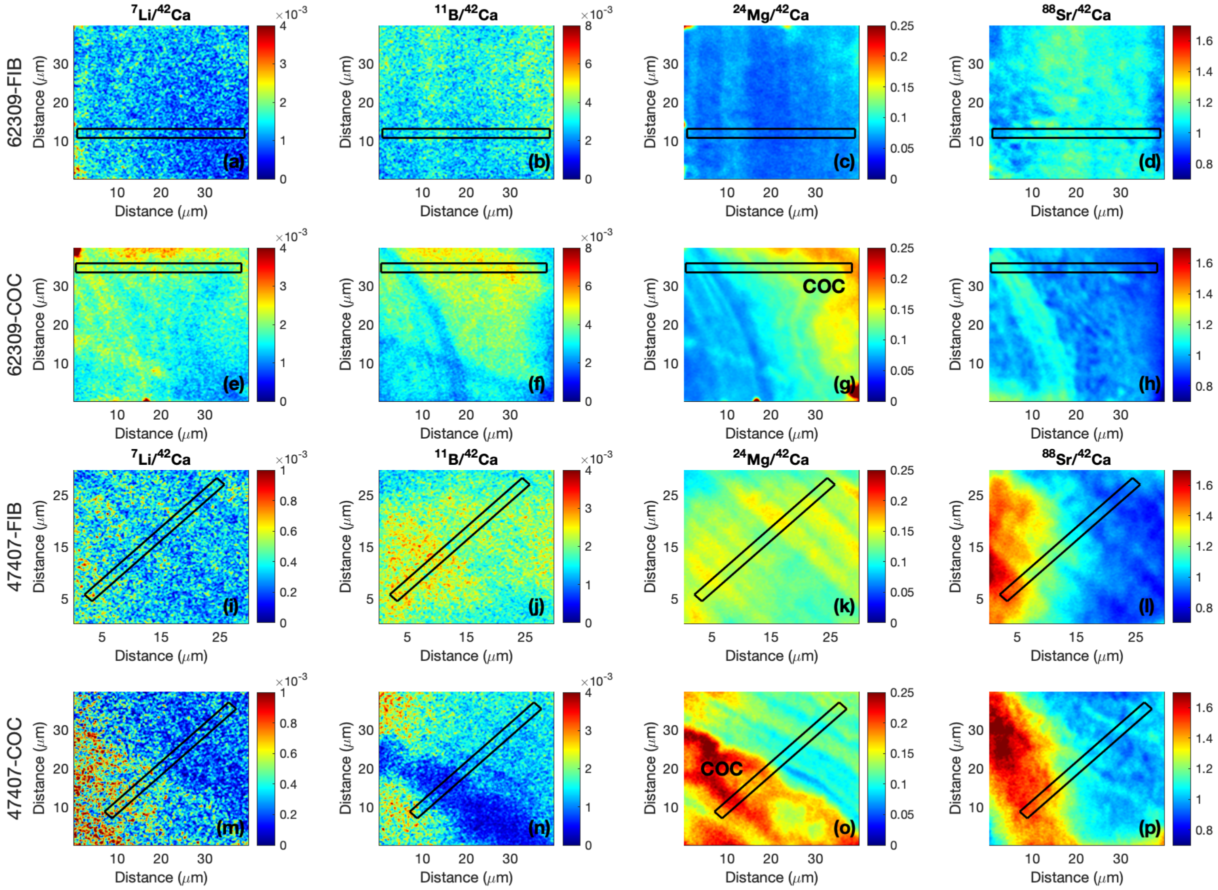

Figure 5 NanoSIMS mapping of coral 62309 and 47407. Each row shows Me/Ca mapping of a 30 or 40 µm spot (512×512 pixels) on the septa of the corals. A 7-pixel smoothing is applied to the raw images to enhance the patterns, especially for Li and B. The top two rows (a–d, e–h) show spots from 62309 and the bottom two rows (i–l, m–p) show spots from 47407. Rows 1 and 3 correspond to a fibrous aragonite (FIB) spot in each coral, while rows 2 and 4 include COC features as evidenced by high Mg/Ca. The images were generated in two separate analytical sessions for the two corals, and the instrument sensitivity was different between the sessions, especially for Li and B. The colorbars for Li/Ca and B/Ca are adjusted for the two corals to maximize the color contrast of each image. The orientations of the growth bands are different for the two corals (vertical for 62309, diagonal for 47407) due to the angles of particular septa when the coral sections were placed into the instrument. The black rectangles in each panel are 30-pixel wide bands through which Me/Ca profiles are generated by L'IMAGE and shown in Figure 6. The high Sr/Ca values on the left edge for 47407 (panel l and p) are most likely a result of surface charging on the sample and do not reflect true Sr/Ca changes in the coral.

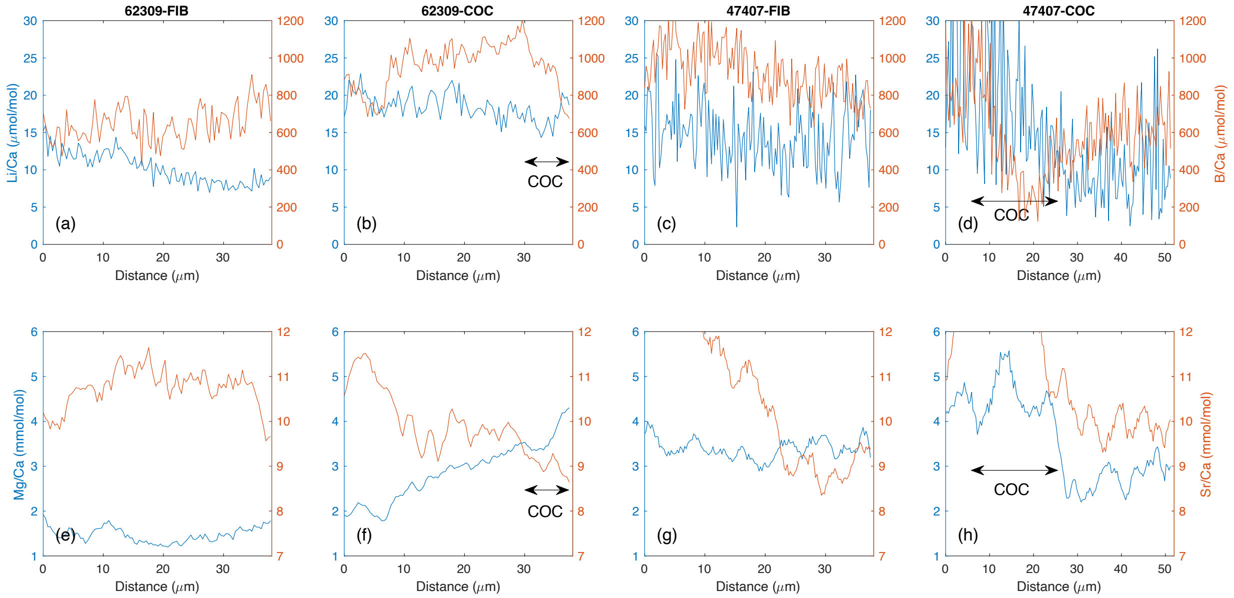

Figure 6 Standardized Me/Ca profiles from transects in NanoSIMS images in Figure 5 produced by L'IMAGE. Each column represents a spot in Figure 6. The top row (a–d) shows Li/Ca on the left axes and B/Ca on the right axes, while the bottom row (e–h) shows Mg/Ca on the left axes and Sr/Ca on the right axes. Significant Me/Ca variations are observed on micron scales in each transect. The COC features show up with significant increase in Mg/Ca and decrease in B/Ca. Sr/Ca for the 47407 spots are cut off at 12 mmol/mol to avoid the high edge values and be consistent with the 62309 spots.

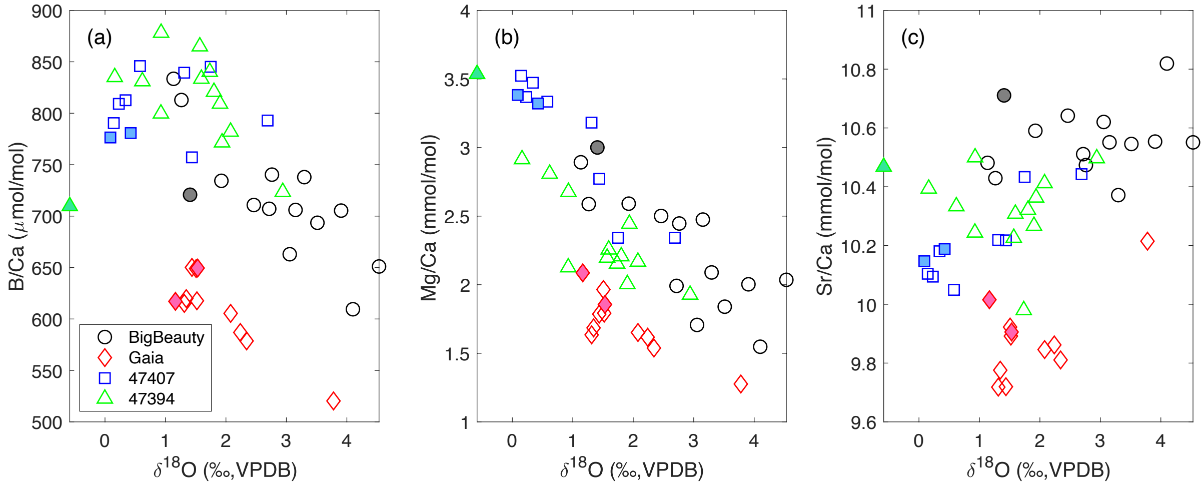

Figure 7 Correlations between δ^{18}O and (a) B/Ca, (b) Mg/Ca and (c) Sr/Ca ratios from micromilled samples (as in Figure 3). The open symbols represent fibrous aragonite while the filled symbols represent the COCs or COC-like structures.

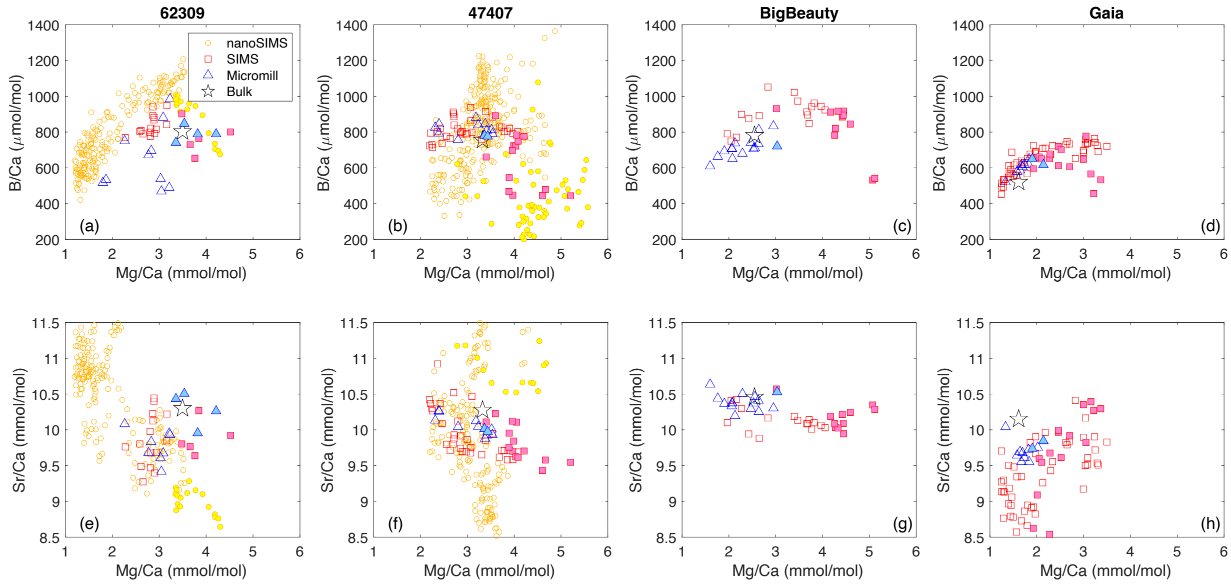

Figure 8 Comparison of Me/Ca correlations across measurement scales in four individual *D. dianthus*. The upper row (a–d) shows Mg/Ca-B/Ca correlations, while the lower row (e–h) shows Mg/Ca-Sr/Ca correlations. Yellow circles represent NanoSIMS data presented in Figure 6. Red squares represent SIMS data, most of which are presented if Figure 4. Blue triangles represent micromill data, most of which are presented in Figure 3. Black stars represent the bulk composition measured for each coral. Open symbols represent aragonite fibers and filled symbols represent COCs or COC-like structures identified on each measurement scale.

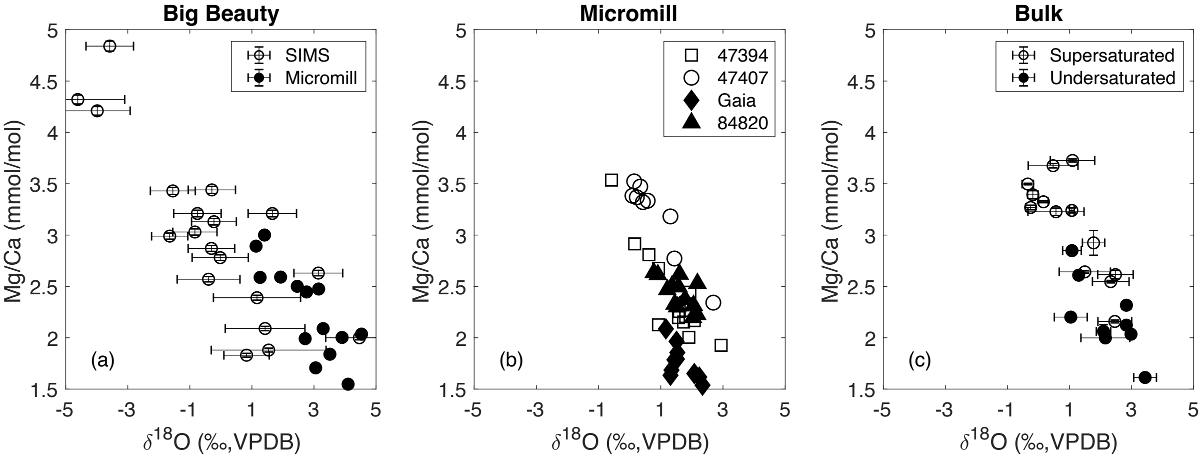

Figure 9 Mg/Ca–δ^{18}O correlation across measurement scales. (a) SIMS and micromill data of Big Beauty. The SIMS data (open circles) are plotted with 2 standard errors. The micromill data (filled circles) have errors smaller than the symbol size. (b) Micromill data of four individual *D. dianthus*. 47394 (open squares) and 47407 (open circles) are from supersaturated seawater, while Gaia (solid diamonds) and 84820 (solid triangles) are from undersaturated seawater. The measurement errors are smaller than the symbols. (c) Mg/Ca and δ^{18}O of bulk coral samples. Each point is a bulk sample of an individual *D. dianthus*. Open symbols and filled symbols are corals from supersaturated and undersaturated seawater respectively. The error bars are 2 SD of replicate measurements of multiple aliquots of the bulk powder.

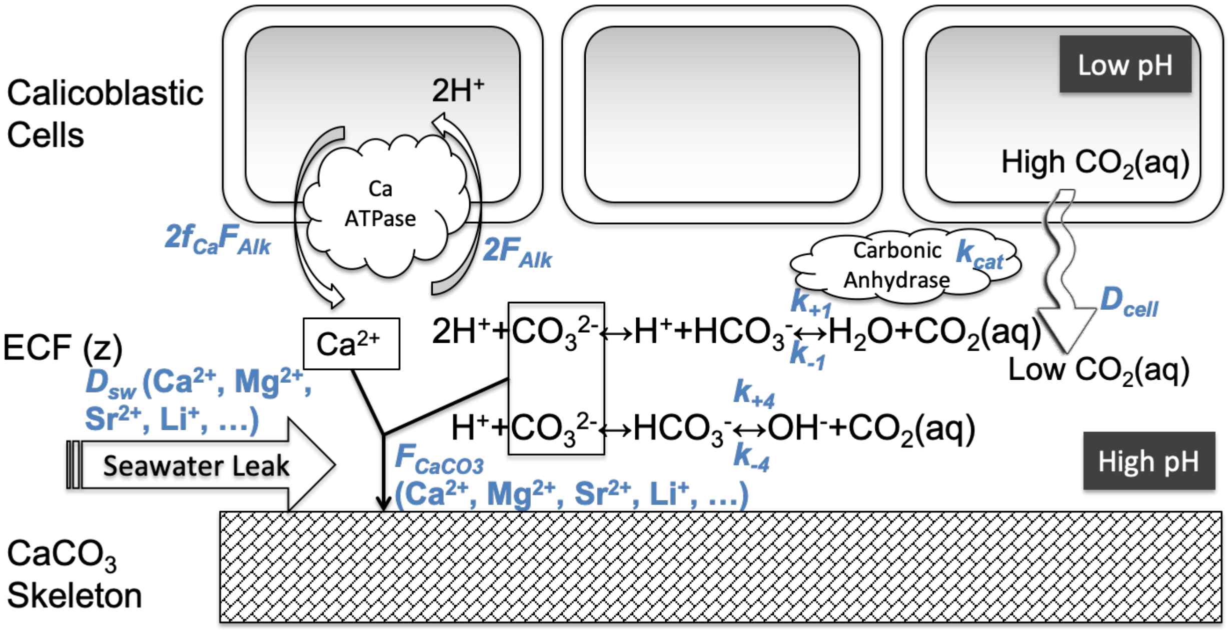

Figure 10 Schematic diagram of the coral biomineralization model. The dynamics of carbonate chemistry and stable isotope fractionation are the same as in Chen et al. (2018). Metal cations are added to the model, with a source from seawater transport (with rate of D_{sw}) and sink by coprecipitation with $CaCO_3$. The dimension of the ECF is z=10 µm, and the seawater turnover timescale is $\tau_{sw} = z/D_{sw}$.

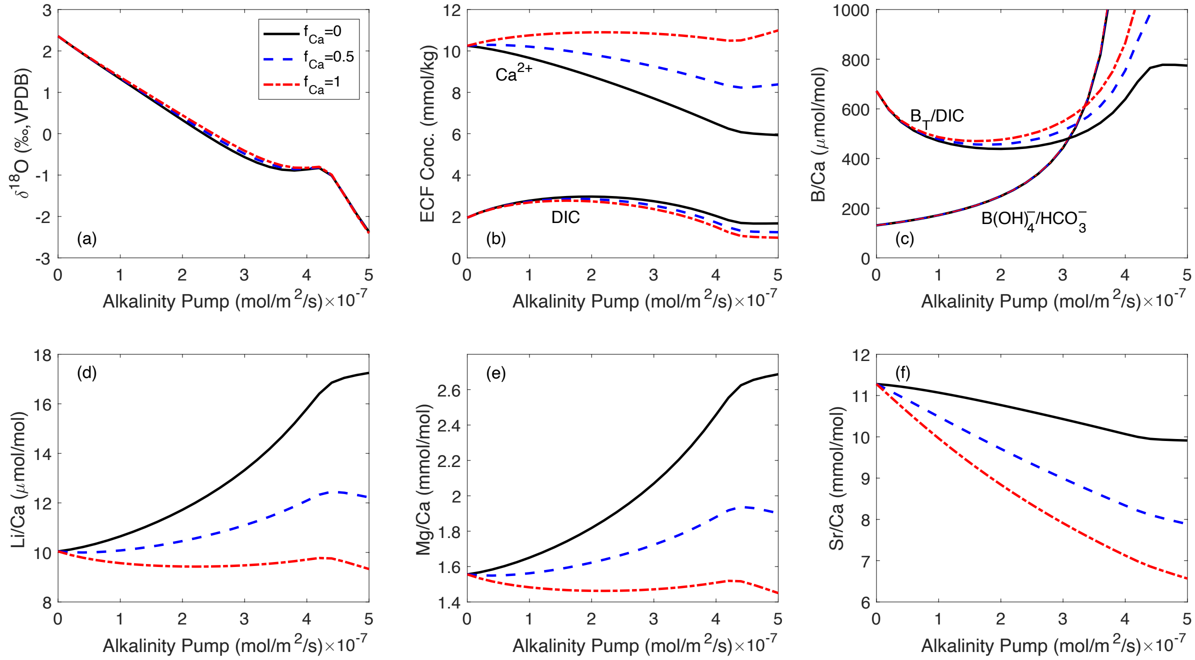

Figure 11 Model output of isotope and Me/Ca tracers vs. alkalinity pump rates. Each point on a model curve is a steady state solution to a prescribed alkalinity pump rate with ambient seawater as the initial condition (5°C, 500 m, 2150 μeq/kg Alk, 2000 μmol/kg DIC). Panel (a) shows $\delta^{18}O$ of the skeleton, panel (b) shows [Ca^{2+}] and DIC in the ECF, and panels (c)–(f) show B/Ca, Li/Ca, Mg/Ca, Sr/Ca of the skeleton respectively. Constant distribution coefficients are assumed for different elements based on inorganic precipitation experiments (D_B=0.003, Hemming et al., 1995; D_{Sr}=1.33, Gaetani and Cohen, 2006) or empirical fits to coral data ($D_{Li}=4\times10^{-3}$, Montagna et al., 2014; $D_{Mg}=3\times10^{-4}$, Reynaud et al., 2007). Two scenarios are shown for B/Ca corresponding to two different boron incorporation rules, $B(OH)_4^-$ substituting HCO_3^- and total boron substituting total DIC. In each panel, the three curves correspond to a different fraction of Ca^{2+} in the total alkalinity pump (f_{Ca}=0 black solid, f_{Ca}=0.5 blue dashed, f_{Ca}=1 red dash-dot).

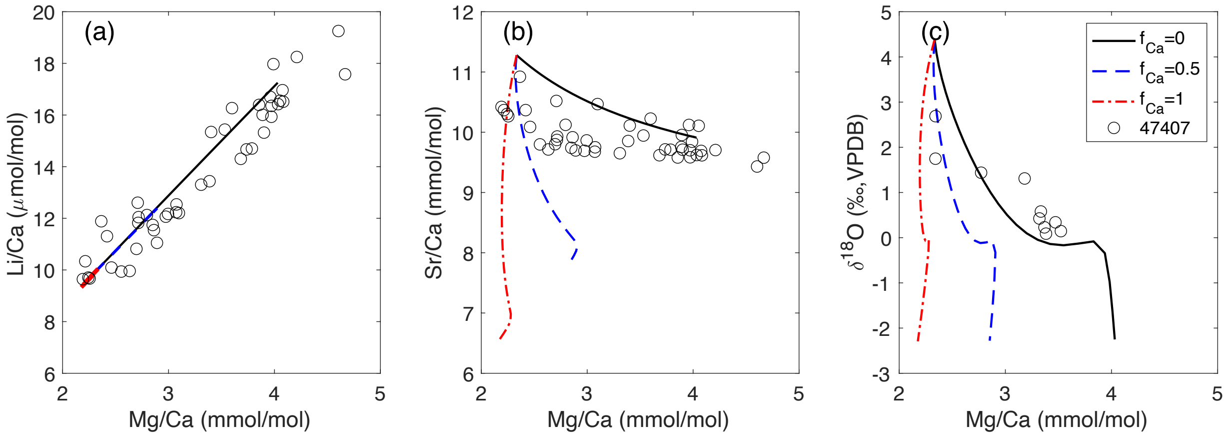

Figure 12 Comparison of model simulations with constant distribution coefficients to tracer data in coral 47407. SIMS data are shown in panels (a) and (b), while micromill data are shown in panel (c). Different curves correspond to different fractions of Ca^{2+} pump in total alkalinity pump. The distribution coefficients used are $D_{Mg}=4.5\times10^{-4}$, $D_{Li}=4\times10^{-3}$, $D_{Sr}=1.33$ respectively. D_{Li} and D_{Sr} are the same as in Figure 9, while D_{Mg} is adjusted to fit the data.

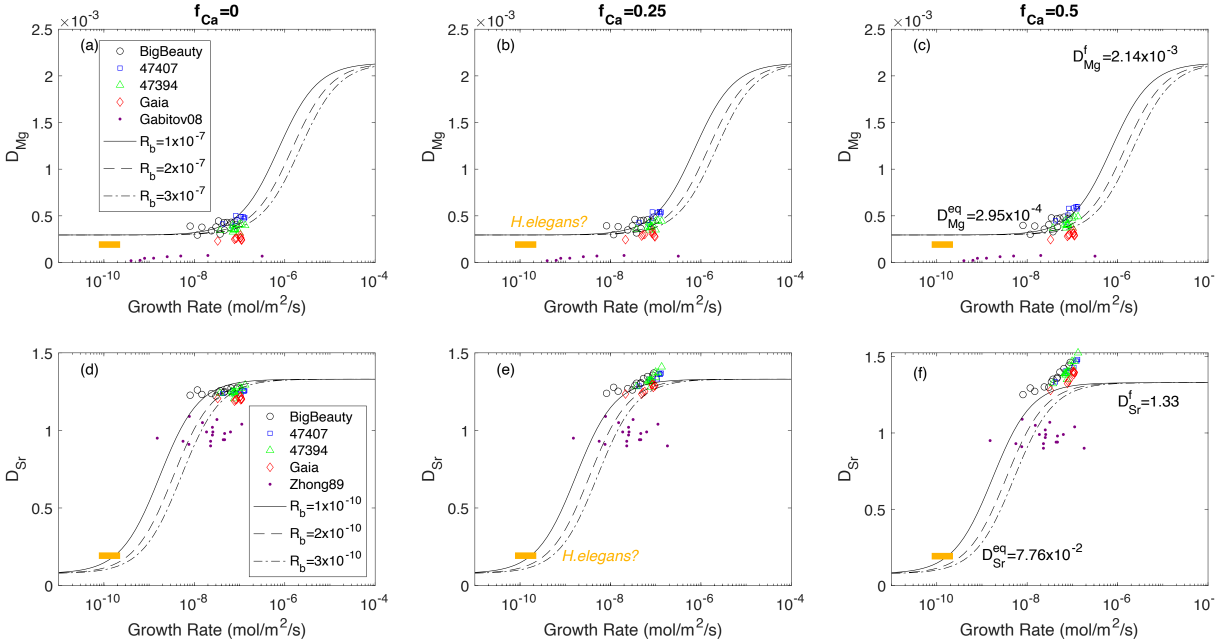

Figure 13 Growth rate dependence of D_{Mg} (a–c) and D_{Sr} (d–f) in aragonite from deep-sea coral *D. dianthus*, foraminifera *H.elegans* and inorganic experiments. Growth rates on the x-axis are net aragonite growth rates ($R=R_f–R_b$). *H.elegans* data (orange bar) are selected from a temperature range of 4–6°C in Rosenthal et al. (2006). The foraminifera growth rates are calculated with the same rate law as the deep-sea corals and assumes a 50% increase in aragonite saturation in the foraminifera calcifying fluid relative to the ambient seawater, with the same Mg/Ca and Sr/Ca as seawater. We only show the range of estimated values with the orange bar due to many uncertainties involved. Inorganic aragonite data (purple dots) are from Gabitov et al. (2008) for Mg and Zhong and Mucci (1989) for Sr. The sigmoid curves are calculated from Equation (4), with different backward reaction rates (R_b in units of mol/m^2/s). The equilibrium end member at low growth rates are calculated from the lattice strain theory (Blundy and Wood, 1994) following Gaetani and Cohen (2006) ($D_{Mg}^{eq}=2.95\times10^{-4}$, $D_{Sr}^{eq}=0.0776$). The kinetic end member at high growth rates are based on experimentally determined temperature dependence in Gaetani and Cohen (2006) ($D_{Mg}^{f}=2.14\times10^{-3}$, $D_{Sr}^{f}=1.33$). Different columns correspond to f_{Ca} values of 0, 0.25 and 0.5.

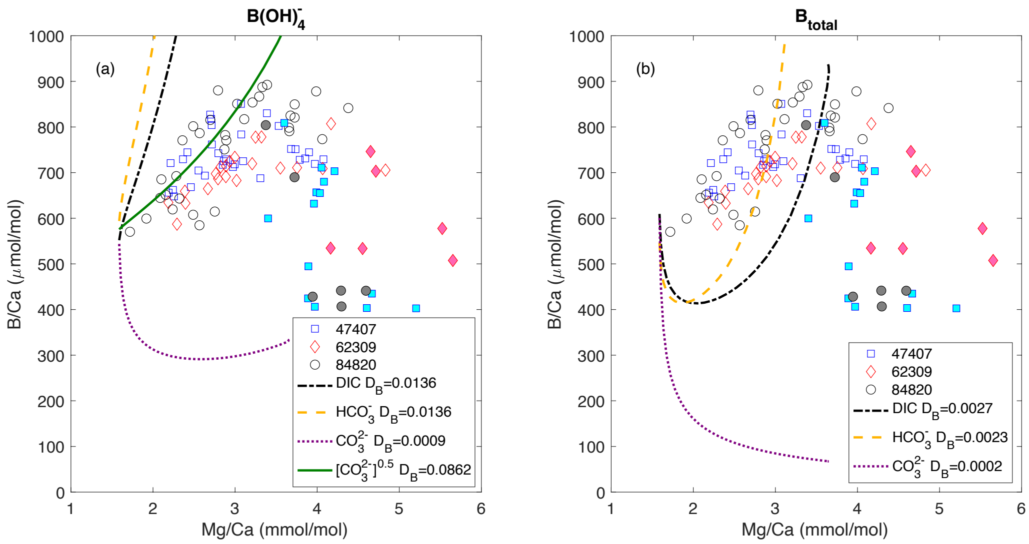

Figure 14 Data-model comparison of Mg/Ca–B/Ca correlation in *D. dianthus*. The data are from SIMS measurements of corals growing close to 5°C. The open symbols show fibrous aragonite while the filled symbols show corresponding COCs of individual corals. Panel (a) shows model results assuming B(OH)$_4^-$ is the species incorporated into the aragonite, while panel (b) shows model results assuming all boron gets incorporated. Different model curves correspond to different DIC species being substituted by boron (DIC with black dash-dot line, HCO$_3^-$ with orange dashed line, CO$_3^{2-}$ with purple dotted line, $[CO_3^{2-}]^{0.5}$ with green solid line). The boron distribution coefficients (D_B) are adjusted to match the data at the lowest Mg/Ca. Mg/Ca are modeled with f_{Ca}=0.1 with growth rate dependence of D_{Mg} at $R_b=2\times10^{-7}$ mol/m^2/s (see Figure 13).

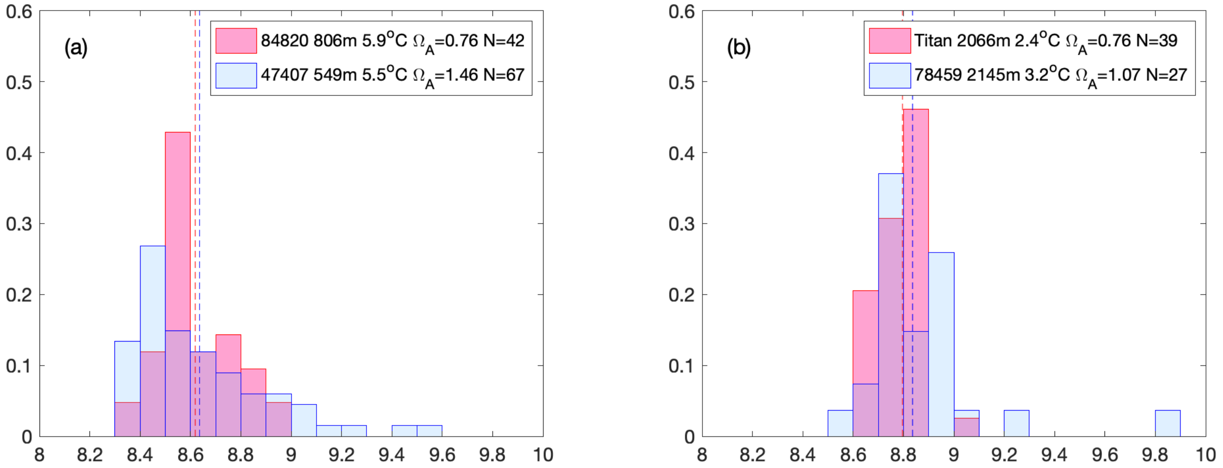

Figure 15 Histogram of ECF pH in *D. dianthus* derived from δ^{18}O measurements (this study and Adkins et al., 2003) and the biomineralization model. Panel (a) shows two corals from the thermocline, and panel (b) shows two corals from >2000m depth. In each panel, one coral is from supersaturated seawater (blue) and the other is from undersaturated seawater (red). The dashed lines show the ECF pH corresponding to the mean δ^{18}O composition of each coral.